

# Knocking out C9ORF72 Exacerbates Axonal Trafficking Defects Associated with Hexanucleotide Repeat Expansion and Reduces Levels of Heat Shock Proteins

Masin Abo-Rady,<sup>1,11</sup> Norman Kalmbach,<sup>2,11</sup> Arun Pal,<sup>3</sup> Carina Schludi,<sup>4</sup> Antje Janosch,<sup>5</sup> Tanja Richter,<sup>6</sup> Petra Freitag,<sup>7</sup> Marc Bickle,<sup>5</sup> Anne-Karin Kahlert,<sup>7</sup> Susanne Petri,<sup>2</sup> Stefan Stefanov,<sup>1</sup> Hannes Glass,<sup>3,8</sup> Selma Staeger,<sup>2</sup> Walter Just,<sup>6</sup> Rajat Bhatnagar,<sup>9</sup> Dieter Edbauer,<sup>4</sup> Andreas Hermann,<sup>1,3,8,10</sup> Florian Wegner,<sup>2,12,\*</sup> and Jared L. Sternecker<sup>1,12,\*</sup>

<sup>1</sup>Technische Universität Dresden, Center for Regenerative Therapies TU Dresden (CRTD), 01307 Dresden, Germany

<sup>2</sup>Department of Neurology, Hannover Medical School, 30625 Hannover, Germany

<sup>3</sup>Department of Neurology, Technische Universität Dresden, 01307 Dresden, Germany

<sup>4</sup>German Center for Neurodegenerative Diseases (DZNE) and Munich Cluster for System Neurology (SyNergy), 81377 Munich, Germany

<sup>5</sup>Max Planck Institute of Molecular Cell Biology and Genetics, 01307 Dresden, Germany

<sup>6</sup>Institute of Human Genetics, University of Ulm, 89081 Ulm, Germany

<sup>7</sup>Institut für Klinische Genetik, Medizinische Fakultät Carl Gustav Carus, Technische Universität Dresden, 01307 Dresden, Germany

<sup>8</sup>Translational Neurodegeneration Section "Albrecht-Kossel", Department of Neurology and Center for Transdisciplinary Neurosciences Rostock (CTNR), University Medical Center Rostock, University of Rostock, 18147 Rostock, Germany

<sup>9</sup>Verge Genomics, San Francisco, CA 94080, USA

<sup>10</sup>German Center for Neurodegenerative Diseases (DZNE) Rostock/Greifswald, 18147 Rostock, Germany

<sup>11</sup>Co-first author

<sup>12</sup>Co-senior author

\*Correspondence: [wegner.florian@mh-hannover.de](mailto:wegner.florian@mh-hannover.de) (F.W.), [jared.sternecker@tu-dresden.de](mailto:jared.sternecker@tu-dresden.de) (J.L.S.)

<https://doi.org/10.1016/j.stemcr.2020.01.010>

## SUMMARY

In amyotrophic lateral sclerosis (ALS) motor neurons (MNs) undergo dying-back, where the distal axon degenerates before the soma. The hexanucleotide repeat expansion (HRE) in *C9ORF72* is the most common genetic cause of ALS, but the mechanism of pathogenesis is largely unknown with both gain- and loss-of-function mechanisms being proposed. To better understand *C9ORF72*-ALS pathogenesis, we generated isogenic induced pluripotent stem cells. MNs with HRE in *C9ORF72* showed decreased axonal trafficking compared with gene corrected MNs. However, knocking out *C9ORF72* did not recapitulate these changes in MNs from healthy controls, suggesting a gain-of-function mechanism. In contrast, knocking out *C9ORF72* in MNs with HRE exacerbated axonal trafficking defects and increased apoptosis as well as decreased levels of HSP70 and HSP40, and inhibition of HSPs exacerbated ALS phenotypes in MNs with HRE. Therefore, we propose that the HRE in *C9ORF72* induces ALS pathogenesis via a combination of gain- and loss-of-function mechanisms.

## INTRODUCTION

Amyotrophic lateral sclerosis (ALS) is a devastating neurodegenerative disease characterized by the progressive loss of motor neurons (MNs). Neurodegeneration proceeds in a dying-back manner, starting with the distal followed by the proximal axon, and finally MN soma death (Naumann et al., 2018). None of the currently available drugs meaningfully delay pathogenesis and new therapeutics are urgently needed.

The most common known genetic cause of ALS is a GGGGCC hexanucleotide repeat expansion (HRE) within the first intron of the gene *C9ORF72*. Approximately 40% of familial and 5% of sporadic ALS cases have an HRE in *C9ORF72* (Majounie et al., 2012). Thus, understanding the pathogenesis of *C9ORF72*-ALS, particularly in the distal axon, could lead to more effective treatments for many ALS patients.

*C9ORF72*-ALS is inherited in an autosomal dominant manner, but the precise mechanism of pathogenesis is un-

clear. At least two studies have assessed *C9ORF72* protein levels in patient brain tissue and demonstrated that *C9ORF72* protein levels are reduced in patients with HRE (Frick et al., 2018; Waite et al., 2014), which is consistent with reports that RNA levels are also reduced (Gijssels et al., 2012). Thus, one of the first hypotheses was that haploinsufficiency leading to a loss-of-function (LOF) mechanism may contribute to ALS and one report showed that reducing *C9ORF72* levels in zebrafish resulted in motor defects (Ciura et al., 2013). However, multiple reports of genetic knockouts (KOs) in zebrafish and mice showed no evidence of MN degeneration and ALS pathology (Hruscha et al., 2013; Jiang et al., 2016). Subsequently, it was discovered that HRE is translated via a non-canonical form of translation called repeat-associated non-ATG (RAN) translation, resulting in neurotoxic dipeptide repeat proteins (DPRs). This has led to the currently predominant idea of a toxic gain-of-function (GOF) causing *C9ORF72*-ALS. However, the majority of mouse models overexpressing HRE or DPRs failed to develop ALS symptoms, in particular





dying-back pathology, even though the mice showed significant levels of DPR proteins (Chew et al., 2015). Thus, both KO and overexpression mouse models could not recapitulate ALS phenotypes, arguing against simple LOF or GOF models and raising the need of a human disease model. A cooperation of LOF and GOF mechanisms driving *C9ORF72*-ALS pathogenesis was recently suggested (Shi et al., 2018). Yet, to date, no model is available that combines both LOF and GOF approaches endogenously.

Here, we used CRISPR/Cas9n gene editing to generate isogenic human induced pluripotent stem cells (iPSCs) and differentiated them into MNs for disease modeling, to better understand the mechanism by which the HRE in *C9ORF72* causes ALS. We observed that MNs with the HRE showed decreased axonal trafficking, increased stress granule (SG) formation and significant transcriptome alterations compared with gene corrected MNs. To test the possibility of an LOF, we generated a *C9ORF72* KO using a healthy control line. However, MNs lacking *C9ORF72* protein showed no significant transcriptomic changes compared with isogenic controls, and axonal trafficking was similar in both wild-type (WT) MN lines (wtKO), suggesting that the HRE does not cause ALS via a simple LOF mechanism. However, rather than a simple GOF, it is possible that reduction of *C9ORF72* protein levels exacerbates a toxic GOF associated with HRE. To test this, we generated iPSCs having both an HRE as well as *C9ORF72* KO. We observed that those MNs showed increased apoptosis, disrupted axonal trafficking and aberrant transcriptome expression compared with MNs with HRE alone. Interestingly, these altered phenotypes were associated with decreased production of heat shock proteins (HSPs), particularly HSP70 as well as DNAJA4, a member of the HSP40 family, rather than increased DPR protein levels. Therefore, we propose that the HRE causes MN degeneration primarily via a toxic GOF that is exacerbated in HRE + *C9ORF72* KO MNs, which is associated with reduced levels of HSPs.

## RESULTS

### Generation of Isogenic iPSCs for Modeling *C9ORF72*-ALS

One of the critical outstanding questions is whether an HRE in *C9ORF72* cause degeneration of human MNs via an LOF or a toxic GOF. To answer this question, we generated a series of isogenic iPSCs. To test if MN degeneration is caused by reduced levels of *C9ORF72* protein, we generated a KO of *C9ORF72* in WT cells using a quadruple Cas9n-nickase (Cas9n) approach that introduced two different double-strand breaks surrounding the translational start codon in exon 2, which is used for all isoforms of *C9ORF72* (Figure 1A). Cas9n was chosen because two different Cas9

proteins must cut in close proximity on opposing DNA strands to introduce a double-strand break. Guide RNAs were selected that would, together, only cut once in the genome, thus eliminating off-target effects. PCR-based genotyping was initially used to confirm deletion of the start codon of *C9ORF72* (Figure 1B). The resulting iPSCs were designated wtKO.

It is also possible that the HRE in *C9ORF72* cause ALS in a GOF manner. To test this, we used CRISPR-Cas9n-mediated gene editing to correct the HRE in iPSCs from two different ALS patients with heterozygous HRE in *C9ORF72* using a donor vector that contained the WT length of three repeats (Figure 1C). Unmodified ALS patient-derived iPSCs were designated C9-1 and C9-2, and their gene corrected isogenic lines were designated C9GC-1 and C9GC-2 (Figure S1A). Repeat-primed PCR demonstrated the presence of the HRE in C9-1 and C9-2, but not in C9GC-1 and C9GC-2 iPSCs (Figures 1D and S1C). Southern blotting validated these results and determined repeat length (Figure S1B). Finally, amplicon length demonstrated C9GC-1 and C9GC-2 iPSCs were heterozygous, containing 5/3 and 2/3 repeats, respectively (Figure S1D).

Finally, we hypothesized that reducing *C9ORF72* protein levels could exacerbate the pathological effects of a GOF. To test this, we used a quadruple-nickase approach to delete the translational start codon in an ALS patient iPSC line, resulting in retained repeat expansion in combination with a loss of *C9ORF72* protein. These gene-edited iPSCs are hereafter called C9 + KO-1 and C9 + KO-2 (Figure 1E). PCR-based genotyping confirmed the presence of the deletion in *C9ORF72* (Figure 1B).

qRT-PCR analysis was used to characterize the effects of gene editing on the expression levels of isoforms of *C9ORF72* as well as antisense RNA levels. Differentiated MNs from all iPSC lines expressed comparable levels of isoform 1, which contains the HRE (Figures S2A and S2B), as well as isoform 2, which encodes the long form of *C9ORF72* protein (Figures S2A–S2C). Isoform 3 was not detected. Antisense transcripts were detected in all differentiated cultures of MNs, but no significant differences were observed (Figure S2D).

Capillary electrophoresis was used to quantify the levels of *C9ORF72* protein in differentiated MNs (Figure 1F). We observed considerable variation in the levels of *C9ORF72* protein. Relative to GAPDH, the levels in WT varied by more than 3-fold. Due to one particular data point, the average *C9ORF72* protein levels was higher in WT compared with C9-1 and C9-2. However, due to the considerable heterogeneity, this difference was not significant, more likely due to stochastic differences between cultures than the HRE. Previous studies reported (Frick et al., 2018; Shi et al., 2018) that patient CNS tissue showed statistically significant reductions in *C9ORF72* compared with

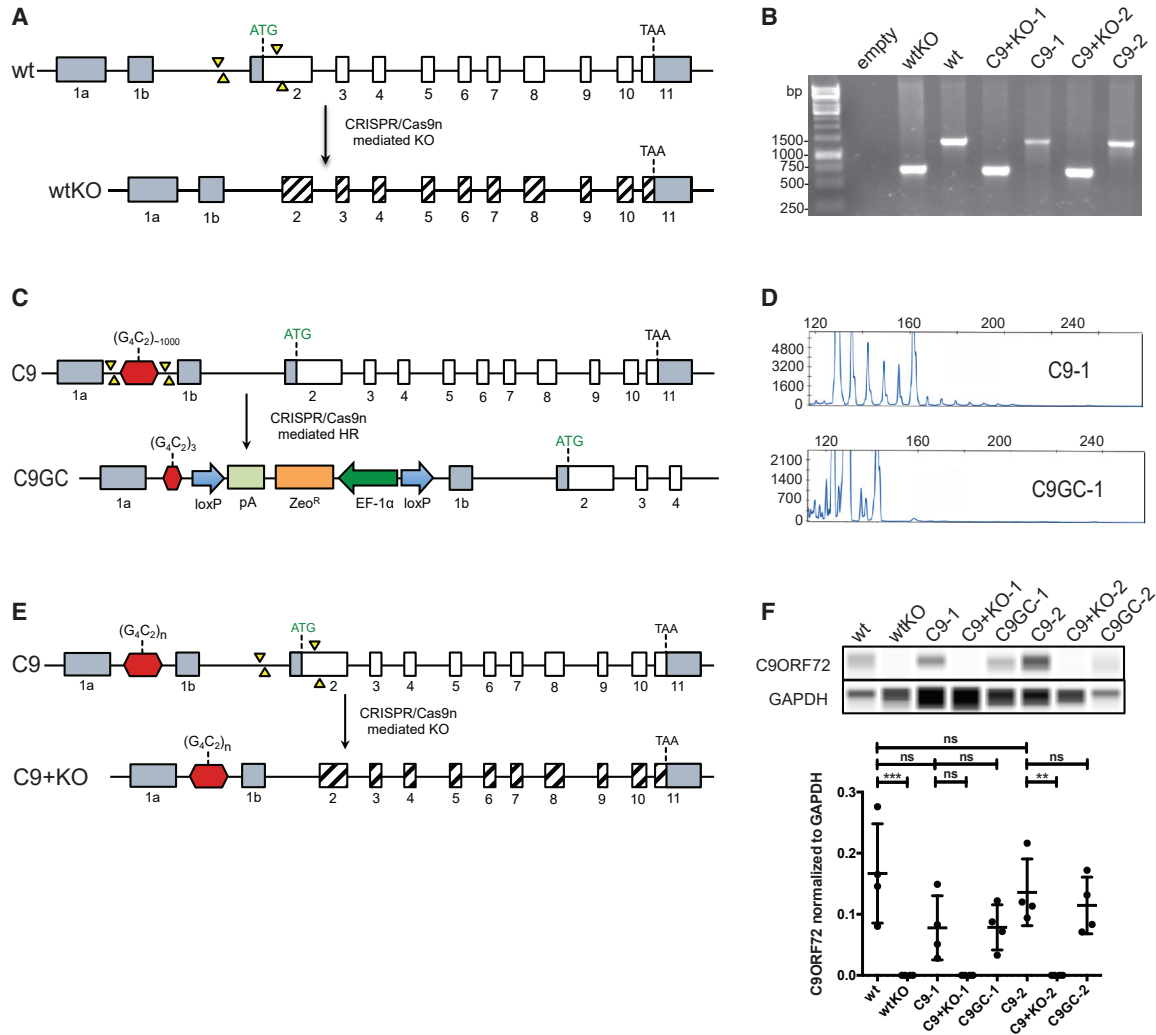


**Figure 1. Generation of Isogenic iPSC Lines**

(A) Strategy for targeting *C9ORF72* to knockout C9ORF72 protein production in WT iPSCs (wtKO). Quadruple Cas9-nickase (Cas9n) introduced two double-strand breaks (yellow arrows). (B) PCR confirmed the deletion in KO iPSC lines. (C) Strategy for gene correction by reducing HRE to WT length of three repeats. (D) Repeat-primed PCR confirmed absence of HRE in C9GC lines. (E) Scheme of KO deletion in iPSCs with HRE in *C9ORF72* (C9 + KO). (F) Capillary electrophoresis confirmed loss of C9ORF72 protein in KO cells. Note that no significant differences between C9-1 and C9-1 in comparison with WT were not significant. N = 4 biological replicates. All values are presented as mean ± SEM. One-way ANOVA showed  $p < 0.05$ . Tukey's post-test for multiple comparisons was performed (\*\* $p < 0.01$ , \*\*\* $p < 0.001$ ). See also [Figures S1–S3](#).

controls. Thus, further reductions in C9ORF72 protein levels are needed in iPSC-derived neurons to recapitulate the conditions observed in patients. Therefore, the comparison between C9 and C9 + KO is of considerable interest, and, in agreement with our genotyping data, C9ORF72 protein was detected in MNs differentiated from C9-1 and C9-2, but not in wtKO, C9 + KO-1 and C9 + KO-2. Of

note, multiple efforts to excise the selection cassette at the *loxP* sites were not successful due to insufficient recombinase activity. As a result of the selection cassette being present, the C9ORF72 protein levels were similar between the gene corrected lines and their respective isogenic parent (Figure 1F). The comparable levels of C9ORF72 protein means that phenotypic differences between C9 and

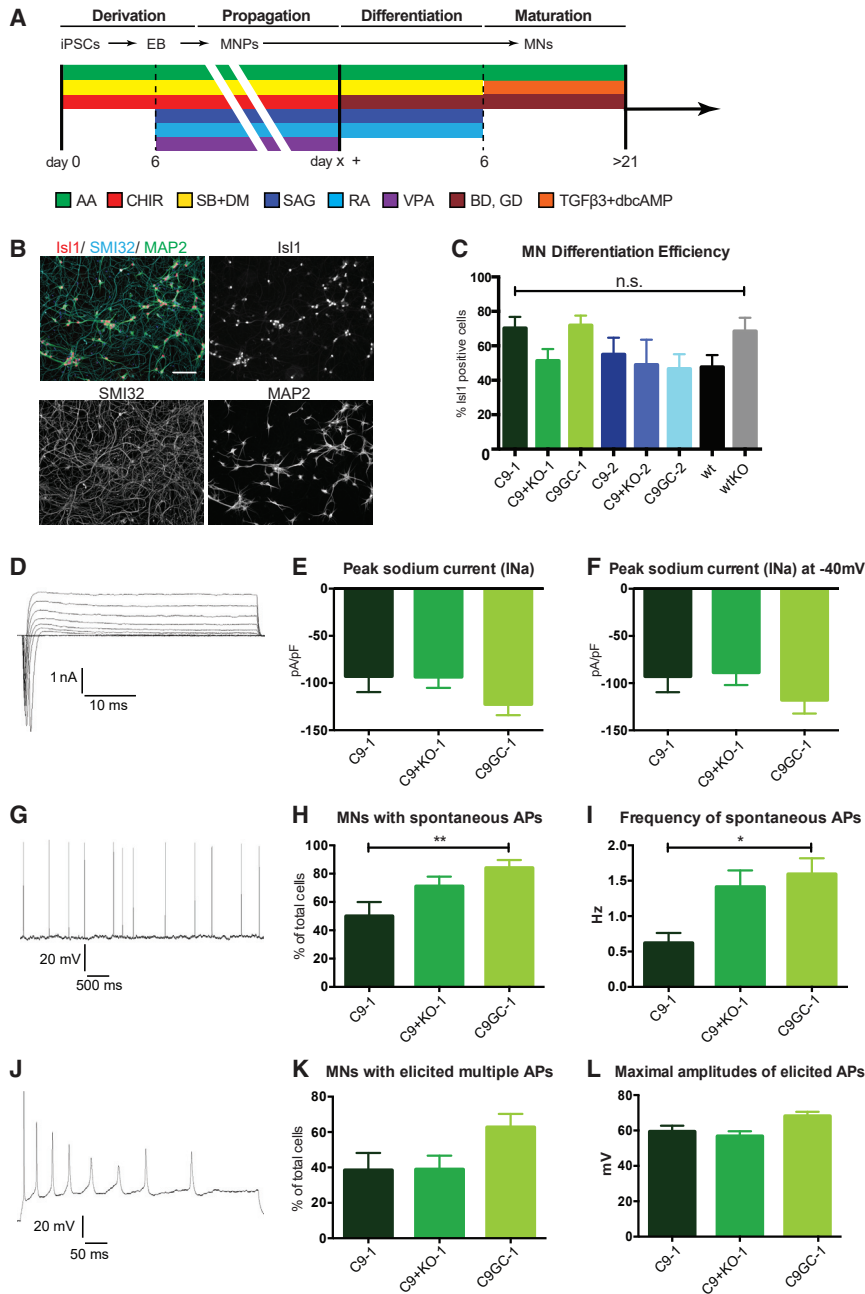


## Figure 2. Differentiation of iPSCs into Functional MNs

(A) Differentiation scheme. (B) MNs express the neuronal marker MAP2 (green) and the MN markers Islet1 (red) and SMI32 (cyan). Scale bar, 100  $\mu$ m.

(C) MN differentiation efficiency is comparable between all cell lines ( $n = 3$  biological replicates). One-way ANOVA showed no statistical significance.

(D–F) Representative voltage-gated sodium inward and potassium outward currents of an MN recorded in whole-cell voltage-clamp mode (D). Peak sodium currents  $I_{Na}$  at maximal amplitude (E) and (F) at  $-40$  mV holding potential.

(G) Recording of a C9GC-1 MN spiking repetitive spontaneous action potentials (APs).

(H and I) Number of spontaneously active MNs (H) and their AP frequency is significantly higher in C9GC-1 than C9-1 MNs (I).

(J) A C9GC-1 MN firing multiple APs upon depolarization in the current-clamp mode. (K and L) The number of MNs with multiple elicited APs (K) and the maximal amplitudes of elicited APs were most pronounced in C9GC-1 cells (L). A minimum of  $n = 32$  cells was measured per line. All values are presented as mean  $\pm$  SEM. Statistical analysis was performed using one-way ANOVA followed by Tukey's post-test for multiple comparisons ( $*p < 0.05$ ,  $**p < 0.01$ ).

See also [Figures S4](#) and [S5](#).

C9GC lines cannot be caused by an LOF mechanism, making them ideal tools to assess possible GOF mechanisms.

Quality control was performed for all iPSC lines. Immunofluorescence confirmed that all lines homogeneously expressed the pluripotent stem cell markers OCT4 and SOX2 ([Figure S3A](#)). Karyotyping was performed for all iPSC lines ([Figure S3B](#)) showing that WT-, wtKO-, C9-1-, and C9-1-derived lines were euploid, but C9-2 contained three copies of chromosome 20, which was equally present in all iPSCs derived from C9-2. However, it will be demonstrated in the

following sections that the majority of observed phenotypes were comparable in both C9-1- and C9-2-derived lines, indicating that the additional chromosome had only a minor effect on ALS phenotypes. These data confirm that the iPSC lines are isogenic and express markers of pluripotency.

## Differentiation of Functional MNs from Isogenic iPSCs

In preparation for modeling ALS, each iPSC line was differentiated into MNs using small molecules ([Figure 2A](#)).



Immunostaining showed that almost all of the cells in the differentiated cultures expressed the neuronal marker MAP2 as well as the MN marker SMI32 (Figure 2B). In addition, approximately 50%–70% of all neurons expressed the MN marker Islet1 (Figure 2B). There was no significant difference between cell lines independent of the genetic background (Figures 2C and S4A). In addition, MAP2 and MN markers SMI32 and CHAT were quantified using qRT-PCR and showed similar expression levels between the isogenic cells derived from C9-1 (Figure S4B). To better characterize the cultures, we performed Eigengene classification of transcriptome data, which identified the cells in these cultures with whole spinal cord with 80% probability (Figure S5A). Analysis of neuronal subtype markers showed that the cultures contained mostly MNs and also spinal interneurons (Figure S5B).

Next, we tested the electrophysiological functionality of the isogenic MNs. Whole-cell patch-clamp analysis demonstrated the development of essential functional properties during MN maturation. There was no significant difference between isogenic WT and wtKO cells (Figures S4C–S4H). Voltage-gated sodium inward and potassium outward currents were comparable between the C9-1-derived cell lines (C9-1, C9 + KO-1, and C9GC-1) although peak sodium current amplitudes were more pronounced in C9GC-1 MNs (Figures 2D–2F). The number of spontaneously active MNs and their action potential (AP) frequency were significantly decreased in C9-1 MNs compared with its isogenic control C9GC-1 (Figures 2G–2I). In addition, the number of MNs with multiple APs and the maximal amplitudes of elicited APs were most pronounced in C9GC-1 MNs (Figures 2J–2L), which is consistent with previously published reports of a hypoexcitability phenotype in HRE carrying MNs (Devlin et al., 2015; Sareen et al., 2013).

Interestingly, Devlin et al. (2015) reported a switch from hyperexcitability (Wainger et al., 2014) to hypoexcitability during differentiation of iPSC-derived MNs with mutations in the genes *TARDBP* and *C9ORF72*. Although in a recent study the excitability in mutant *C9ORF72* iPSC-derived MNs, healthy and isogenic controls was not significantly different (Selvaraj et al., 2018), we found a hypoexcitability phenotype in mutant *C9ORF72* MNs (C9-1) compared with their control (C9GC-1), which was also seen in other mutant ALS genotypes (Naujock et al., 2016; Naumann et al., 2018; Zhang et al., 2013).

### Gene Correction and Transcriptome Sequencing Suggests that HRE Induces MN Degeneration via a GOF

As an unbiased approach, we used transcriptome sequencing to determine differences in gene expression and pathways affected by the HRE (Figure 3A). We compared transcriptome profiles of C9-1 and C9-1GC

MNs. A total of 1,235 genes were differentially expressed (Figure 3B) of which the majority were upregulated in C9-1 (Figure S6A). Gene ontology analysis showed enrichment of multiple terms related to ALS pathogenesis, including positive regulation of programmed cell death, DNA damage checkpoint, microtubule organization, and microtubule motor activity (Figures 3E, S6G, and S6I).

Next, the transcriptome of WT and wtKO MNs was analyzed (NCBI GEO: GSE143744). The LOF model predicts that transcriptome changes in wtKO cells compared with WT would be comparable with HRE-associated changes. In contrast, the GOF model predicts HRE-associated changes would not be recapitulated in wtKO neurons compared with WT. We observed that only 135 genes were differentially expressed in wtKO cells compared with WT (Figure 3C). Although there was some overlap with the genes altered in C9 versus C9GC (Figure S6B), gene ontology analysis could not identify any significantly enriched terms. This suggests that *C9ORF72* LOF alone does not cause neurodegeneration.

We hypothesized that reduced levels of *C9ORF72* would exacerbate the pathogenicity of a toxic GOF. To test this, we sequenced the transcriptome of MNs differentiated from C9 + KO-1 iPSCs and compared it to isogenic C9-1 MNs (NCBI GEO: GSE143743). We identified 582 differentially expressed genes (Figure 3D), of which 553 were also differentially expressed between C9GC-1 versus C9-1 (Figure 3E), demonstrating a considerable overlap. Interestingly, most of these overlapping proteins were downregulated in C9 + KO compared with C9 (Figures S6C and S6E). There was some overlap with the genes differentially regulated between WT and wtKO (Figure S6D). Gene ontology analysis showed enrichment for terms related to MN degeneration, including negative regulation of cell death, regulation of apoptosis, microtubule motor activity and neuron projection regeneration (Figures 3G, S6H, and S6J). These results could suggest that *C9ORF72* KO might exacerbate the pathogenicity of HRE. This is underpinned by the fact that rather all differentially expressed genes between C9 and C9 + KO overlap with genes dysregulated in C9GC versus C9, which is, however, not the case vice versa (Figure 3E).

Previously, Selvaraj et al. (2018) reported transcriptome analysis of MNs differentiated from isogenic *C9ORF72* iPSCs. Unexpectedly, we found very little overlap with our results (Figure S6F). However, it is known that *C9ORF72* pathology, phenotypes, and penetrance differ from patient to patient, suggesting that HRE-mediated transcriptome changes are strongly dependent on the genetic background. Interestingly, one of genes downregulated by HRE in both datasets was *DNAJA4*, which is an HSP40 family member, and could suggest that HSPs play an important role in the pathogenesis of *C9ORF72*-ALS.

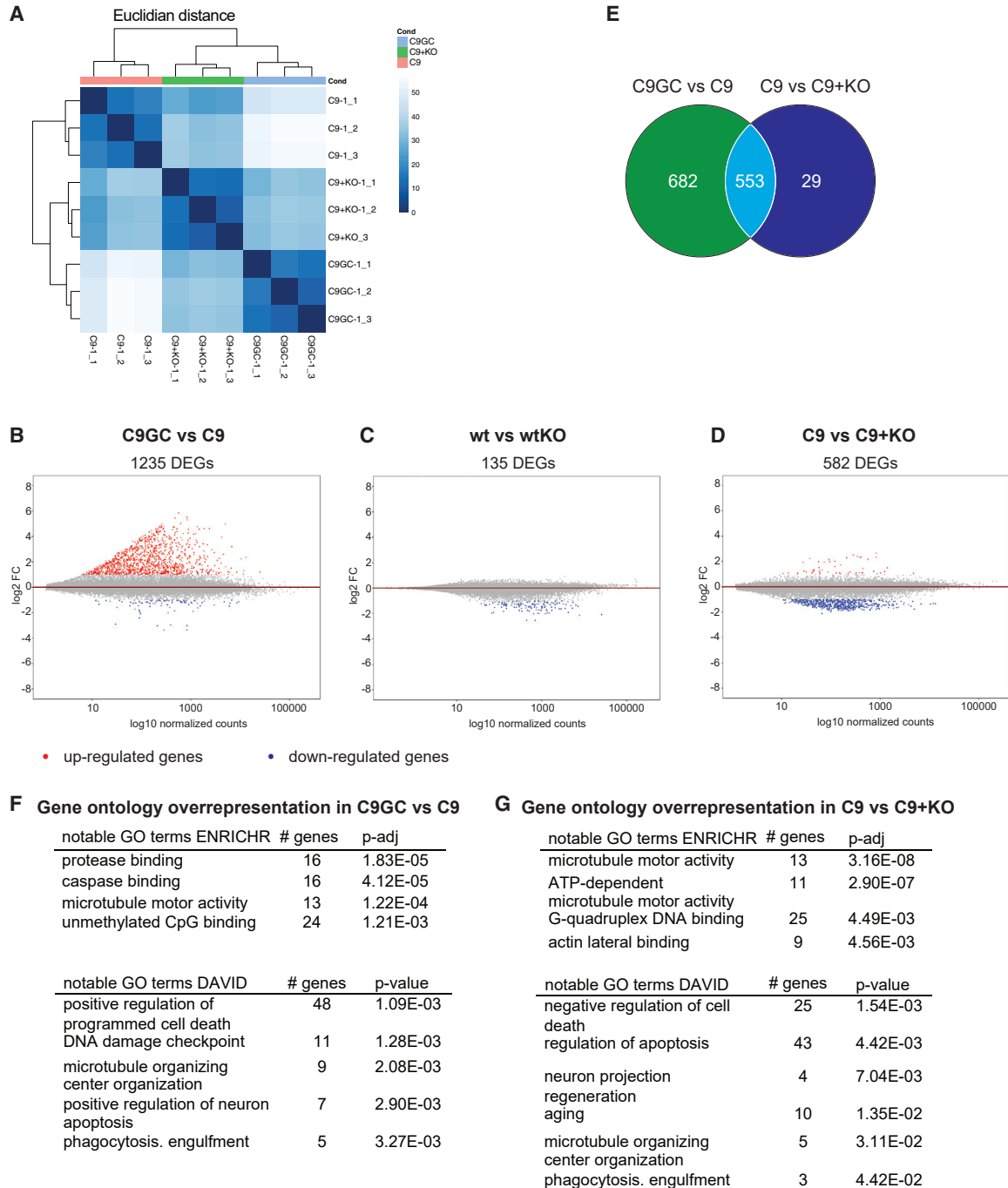


### Figure 3. Transcriptome Analysis of Isogenic MNs

(A) Heatmap and hierarchical clustering of transcriptome results from the indicated MNs.

(B–D) MA plots depict significantly ( $p < 0.05$ ) upregulated (red) and downregulated genes (blue). (B) shows C9GC versus C9, (C) shows wt versus wtKO, and (D) shows C9 versus C9 + KO.

(E) Venn diagram shows numbers of differentially expressed genes (DEGs) between C9GC versus C9 MNs (green), between C9 versus C9 + KO MNs (blue), and the overlap of both comparisons (cyan).

(F and G) Gene ontology studies on DEGs between (F) C9GC versus C9 and (G) C9 versus C9 + KO using ENRICHR (top) and DAVID (bottom). See also Figure S6.

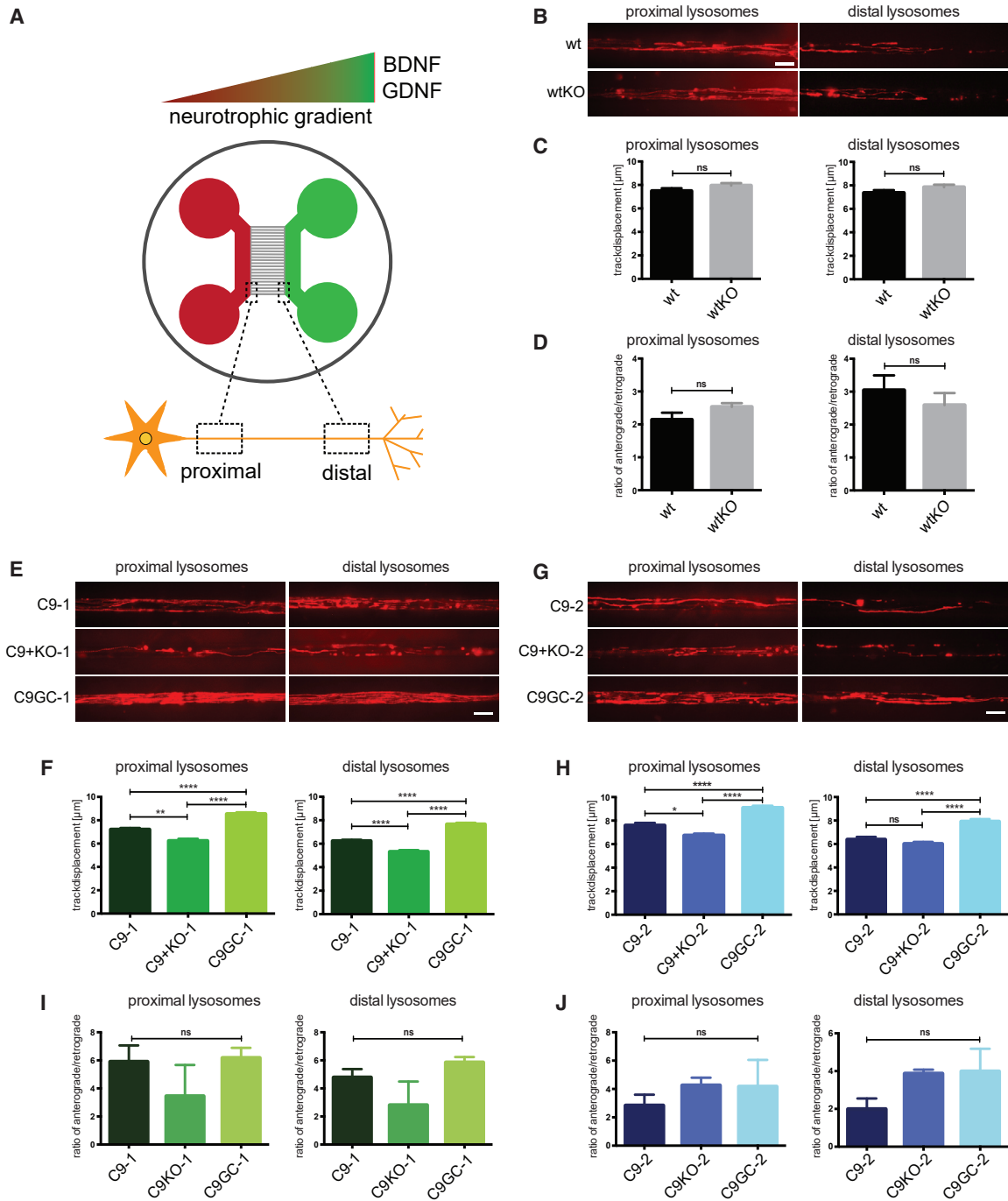


#### Figure 4. Axonal Trafficking Is Altered by the HRE and Loss of C9ORF72

(A) Schematic representation of microfluidic chambers used for live-cell imaging.

(B) Maximum projection for WT and wtKO MNs of 400 frames acquired within a 2-min movie. Higher signal correlates with longer track displacement. Scale bar, 10  $\mu\text{m}$ .

(C and D) Quantification shows (C) track displacement of lysosomes in  $\mu\text{m}$  and (D) direction of trafficking. N = 3 biological replicates; >1,000 lysosomes were analyzed per cell line and per side for all experiments.

(E) Maximum projection for C9-1 MNs. Scale bar, 10  $\mu\text{m}$ .

(F) Quantification shows track displacement of C9-1 lysosomes in  $\mu\text{m}$ .

(G) Maximum projection for C9-2 MNs. Scale bar, 10  $\mu\text{m}$ .

(legend continued on next page)



### HRE Induces Distal Axon Trafficking Defects that Are Exacerbated in Neurons with HRE + C9ORF72 KO

During ALS, MNs undergo dying-back in which distal axon degeneration precedes MN death (Naumann et al., 2018). A possible reason for the distal axon degenerating first is a disruption of axonal transport, which is used to deliver RNA, proteins and even organelles to the synapse to maintain its function. Mutations in motoric proteins, such as KIF5A and DCTN1 have been associated with ALS (Nicolas et al., 2018; Puls et al., 2003) and our transcriptome data suggested that axonal trafficking is affected by HRE as well as HRE + C9ORF72 KO, which could contribute to dying-back pathogenesis. As C9ORF72 protein function is linked to autophagy and lysosomes (Shi et al., 2018), we focused on lysosomal trafficking in MN axons using microfluidic devices. MNs were seeded into one side of the device, defined as “proximal,” and axons grew through channels to the distal side attracted by brain-derived neurotrophic factor (BDNF) and glial cell line-derived neurotrophic factor (GDNF) (Figure 4A). Lysosomes were labeled using Lyso-Tracker, and live imaging of the axons was performed to assess the distance traveled, referred to as track displacement. Similar to our transcriptome data, WT and wtKO cells did not show any differences in the track displacement or directionality of lysosomal trafficking at either the proximal or the distal axon (Figures 4B–4D), suggesting that the HRE does not cause neurodegeneration via a simple LOF.

Next, we assessed axonal trafficking in MNs with the HRE in C9ORF72. We found that MNs from C9-1 and C9-2 showed significantly decreased lysosomal track displacement in distal as well as proximal axons compared with their gene corrected counterparts (Figures 4E–4H). Remarkably, lysosomes in the axons of C9 + KO-1 and C9 + KO-2 showed even shorter track displacement in proximal and distal axons, demonstrating that C9ORF72 KO exacerbated axonal trafficking defects of the HRE. No significant alterations were observed in the directionality of lysosomal trafficking (Figures 4I and 4J). These data demonstrate that the HRE induces degeneration of the distal MN axon before the proximal axon, which is consistent with dying-back pathogenesis.

### C9ORF72 KO Exacerbates MN Degeneration in HRE MNs

In ALS patients, axonal degeneration is followed by the death of the MN soma. Because loss of C9ORF72 protein exacerbates defects in axonal transport in MNs containing

an HRE, we predicted that MNs with HRE and deleted C9ORF72 protein would show the highest levels of apoptosis. Consistent with this idea, our transcriptome data showed that gene ontology terms related to neuronal death and apoptosis were enriched in MNs with HRE + C9ORF72 KO. Thus, we investigated apoptosis in differentiated MNs. To do this, iPSC-derived MNs were cultured for 14 days and immunostained for TUJ1 and the late apoptotic marker cleaved caspase-3 (CC3) (Figure 5A). Quantification showed that CC3 levels in C9 + KO-1 were more than 2-fold of CC3 levels in C9-1 and C9GC-1, which were comparable (Figure 5B). Similarly, C9 + KO-2 showed higher levels of CC3 compared with C9-2 and C9GC-2. These data demonstrate that deleting C9ORF72 protein increases apoptosis in MNs with HRE in C9ORF72.

### DPR Protein Levels Are Associated with HRE but Not Increased by C9ORF72 KO

Transcriptomics and axonal trafficking demonstrate the association of the HRE with a toxic GOF, and DPR proteins translated from HRE-containing RNA are currently the best and most discussed candidate for the toxic GOF. For this reason, we used an ELISA immunoassay to quantify the endogenous levels of poly-GP DPR proteins in differentiated MNs. As expected, no poly-GP protein was detected in WT, wtKO and the gene corrected lines C9GC-1 and C9GC-2 (Figure 5C). In contrast, C9-1 and C9-2 MNs expressed significantly higher levels of poly-GP compared with isogenic controls. However, there was no significant difference in the levels of poly-GP protein between C9-1 and C9-2, despite the different lengths of repeat expansion (C9-1 having ~1,000 repeats; C9-2 having ~750 repeats). Immunostaining was used to validate the presence of DPR proteins in iPSC-derived MNs. In contrast to gene corrected controls, we consistently observed punctate staining in the cytoplasm and neurites of MNs carrying an HRE (Figure 5D). However, the high level of unspecific staining made the immunostaining images difficult to quantify. Interestingly, ELISA results showed that C9 + KO-1 and C9 + KO-2 expressed about 40% less poly-GP protein compared with their respective parental lines (Figure 5C), which is particularly surprising as we previously found that MN degeneration was highest in these lines. This clearly indicates that C9ORF72 KO exacerbates MN degeneration without increasing DPR protein levels and suggests that other factors influence the pathology of C9ORF72-ALS. It is interesting to note that the decrease in DPR levels in C9 + KO versus C9

(H) Quantification shows track displacement of C9-2 lysosomes in  $\mu\text{m}$ .

(I and J) Quantification of direction of lysosomal trafficking. N = 3 biological replicates; >1,000 lysosomes were analyzed per cell line and per side for all experiments. Lysosome trafficking results are shown in (I) for C9-1, C9KO-1, and C9GC-1, and in (J) for C9-2, C9KO-2, and C9GC-2. All values are presented as mean  $\pm$  SEM. One-way ANOVA followed by Tukey's post-test for multiple comparisons was performed (\*\*p < 0.01, \*\*\*p < 0.001, \*\*\*\*p < 0.0001). Tracks were shorter at the distal axon end than on the proximal compartment, consistent with dying-back.



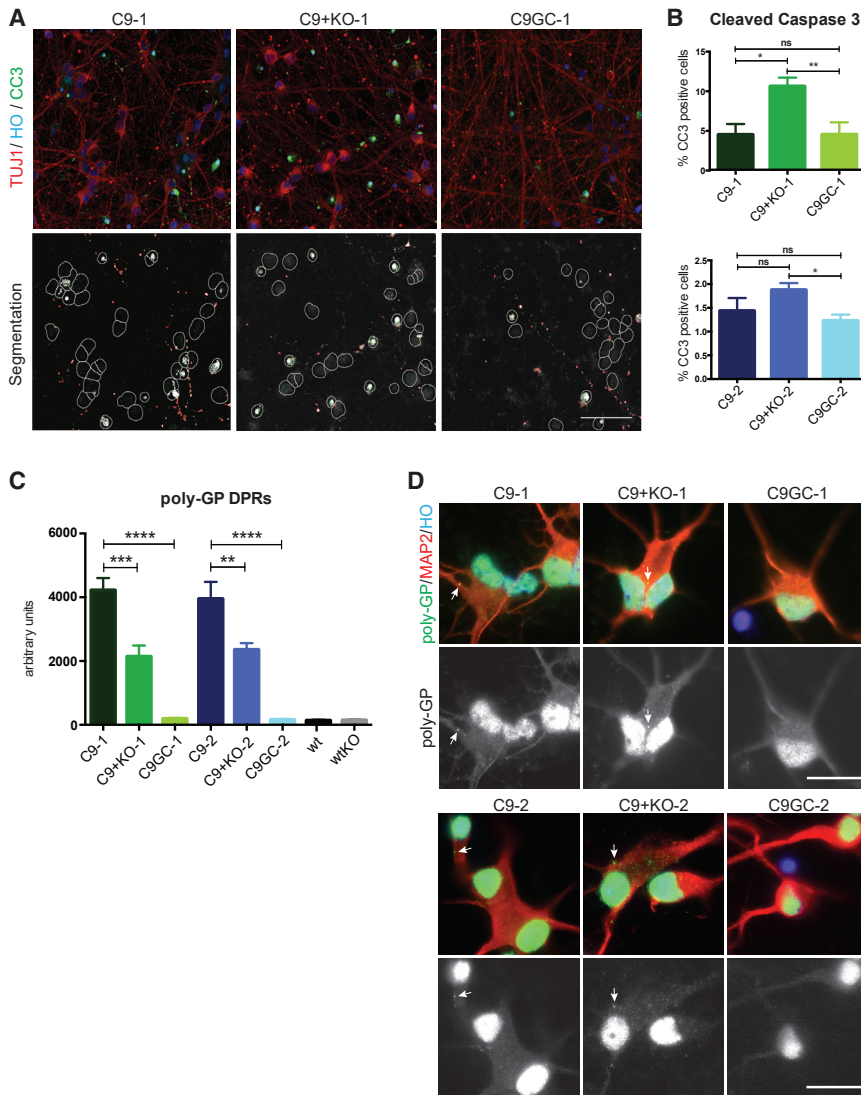


### Figure 5. HRE + *C9ORF72* KO Neurons Show Increased Apoptosis without Increasing DPR Protein Levels

(A) Immunostaining for the indicated markers. Images were segmented using CellProfiler to quantify cleaved caspase-3 (CC3), a marker of apoptosis. Scale bar, 50  $\mu$ m.

(B) C9 + KO MNs show more apoptosis compared with gene corrected C9GC (n = 3 biological replicates).

(C) Quantification of endogenous poly-GP DPR levels using an ELISA assay (n = 7 biological replicates).

(D) Immunostaining for the indicated markers, including MAP2 and poly-GP DPR proteins. Poly-GP peptides could be detected in the cytoplasm of C9 and C9 + KO MNs (indicated by arrows) but not in gene corrected controls. Isogenic cell lines set 1 (left) and set 2 (right). Scale bars, 10  $\mu$ m. All values are presented as mean  $\pm$  SEM. One-way ANOVA followed by Tukey's post-test for multiple comparisons was performed (\*p < 0.05, \*\*p < 0.01, \*\*\*p < 0.001, \*\*\*\*p < 0.0001).

MNs correlates with an apparent reversion in the expression of genes differentially expressed in MNs with HRE (Figures S6A and S6C), suggesting that DPR levels may play a causal role in the expression of many differentially expressed genes in iPSC-derived MNs.

Since *C9ORF72* protein functions in autophagy, we expected that DPR protein levels would be increased instead of decreased. To better understand the possible mechanism for this decrease, we further characterized the deletion present in *C9ORF72* KO cells. The HRE residing in the first intron is normally spliced out of the mature *C9ORF72* mRNA. However, in addition to removing the start codon, the splice acceptor site was also removed (Figure 1E). Thus, we predicted that mature mRNA transcript for *C9ORF72* would contain the HRE. To test this hypothesis, transcriptome reads mapping to the intron were examined and

C9 + KO-1 showed considerably more reads mapping to the intron compared with C9-1 (Figure S7A). A recent report showed retention of intron 1 decreases RAN translation due to the presence of an upstream open reading frame (uORF) (Tabet et al., 2018), but we did not observe any significant difference in the levels of the uORF transcript in C9 + KO MNs compared with C9 (Figure S2E). Nevertheless, it is possible that change in context of the HRE might contribute to the lower DPR levels observed in our C9 + KO-1 and C9 + KO-2 lines. Thus, we argue that a change in RNA splicing is likely responsible for the decrease in DPR protein levels.

### HSP Levels Are Altered by HRE and Exacerbated by *C9ORF72* KO

Next, we sought to identify a possible mechanism by which *C9ORF72* KO exacerbated MN degeneration without



increasing DPR levels. HSPs play a crucial role in the protein quality control system and recently it was shown that HSP70 and HSP40 were critical nodes in the transcriptome network in the frontal cortex of ALS patients with HRE in *C9ORF72* (Prudencio et al., 2015). This led us to hypothesize that *C9ORF72* KO could reduce the levels of specific HSPs, which might exacerbate the toxicity of DPR proteins for MNs. Measuring protein expression of HSP70 family members HSPA1A and HSPA1B using capillary electrophoresis revealed that C9-1 and C9-2 MNs expressed less HSPA1A and significantly less HSPA1B compared with the gene corrected controls C9GC-1 and C9GC-2 (Figures 6A and 6B). This reduction was even greater in C9 + KO-1 and C9 + KO-2. As indicated above, we found that DNAJA4, which is an HSP40 family member that forms complexes with HSP70, was downregulated in MNs with HRE compared with gene corrected controls in our data as well as in the results from Selvaraj et al. (2018). We observed a trend toward decreased DNAJA4 protein in HRE MNs compared with gene corrected, but there was a striking and significant decrease of DNAJA4 protein in *C9ORF72* KO MNs, which showed only 10%–50% of the parental levels (Figure 6C). Therefore, changes in HSP levels correlate with the exacerbated ALS phenotypes, suggesting that they play a critical role in MN degeneration.

#### SG Formation Is Perturbed by HRE and Exacerbated by KO of *C9ORF72*

SGs have been suggested to be crucibles of ALS pathogenesis (Li et al., 2013). They are membraneless organelles formed by liquid-liquid protein phase separation. Although both DPR proteins as well as HSPs play critical roles in SG formation and maintenance, we predicted that SGs might be affected by the loss of *C9ORF72* protein in MNs containing the HRE. Therefore, we assessed SG formation using our isogenic MNs. Differentiated MNs were treated for 1 h with 0.5 mM sodium arsenite to induce SG formation, which were assessed using immunostaining for the SG marker eukaryotic translation initiation factor 3 (eIF3) in combination with the neuronal marker MAP2. eIF3-positive SGs were observed in the cytoplasm and often in perinuclear regions (Figure 6D). The mean eIF3 intensity was comparable between the lines (Figure 6E). Quantification showed a significant increase of the number of SGs per cell with an HRE compared with gene corrected controls (Figure 6F). Importantly, the number of SGs per cell was even higher in cells with HRE + *C9ORF72* KO, which is consistent with our previous results that *C9ORF72* KO exacerbates ALS-associated phenotypes of HRE MNs. Therefore, we suggest that membraneless compartments, such as SGs, could be a point of pathological convergence of DPR proteins and reduced HSP levels leading to MN degeneration in *C9ORF72*-associated ALS.

#### Inhibition of HSPs Exacerbates Axonal Trafficking Defects and Induces Apoptosis in MNs with HRE

C9 + KO MNs showed decreased HSP levels as well as exacerbated ALS phenotypes compared with C9 MNs, leading us to hypothesize that inhibiting HSPs would increase degeneration of C9 MNs. To test this, axonal trafficking was assessed using iPSC-derived MNs with the HRE treated with 200  $\mu$ M KNK437, which inhibits the synthesis of HSPs, including HSP70 as well as HSP40 (Yokota et al., 2000). We observed that C9-1 as well as C9-2 MNs showed significantly reduced lysosomal track displacement in the proximal and distal axons (Figure 7A). In addition, the directionality of lysosomal trafficking was severely affected (Figure S7B). To confirm that HSPs are causally linked to the survival of MNs with HRE, we assessed apoptosis using immunostaining for CC3 (Figure 7B). We observed a significant and dose-dependent increase in CC3 staining of iPSC-derived C9-1 and C9-2 neurons treated with KNK437 (Figure 7C). These data demonstrate that HSPs play a critical role in MN survival and that knocking out *C9ORF72* exacerbates ALS phenotypes in iPSC-derived MNs with HRE, which is associated with reduced levels of specific HSPs.

#### DISCUSSION

To prevent ALS onset and progression, it is essential to prevent the degeneration of motor axons in addition to soma. This was illustrated using mice with mutant *SOD1* where a KO of the gene *Ppif*, which encodes cyclophilin D, had no impact on disease onset, progression or survival although *SOD1* protein aggregation was reduced and increased numbers of MN soma were protected in the spinal cord (Parone et al., 2013). Here, we demonstrate that axonal degeneration is a feature of the degeneration of MNs with HRE in *C9ORF72*, which is the most common mutation known to cause ALS.

Currently, it is not fully understood whether HRE in *C9ORF72* cause ALS via LOF or GOF. Thus, isogenic control iPSC lines are powerful tools enabling the generation of MNs with specific genotypes in a defined genetic background to identify pathological mechanisms (Selvaraj et al., 2018). We produced a complete set of isogenic human iPSC-derived MNs to assess the contributions of LOF and GOF to ALS phenotypes. Because *C9ORF72* transcript levels are reduced by the HRE, which can also retain the repeat expansion in ALS patients (Niblock et al., 2016), it is possible that both mechanisms contribute to pathogenesis. To test the possibility that reducing *C9ORF72* protein levels could exacerbate ALS pathogenesis in MNs with HRE, we created isogenic MNs with a *C9ORF72* KO as well as HRE. Importantly, this model produces DPR protein at endogenous levels and without any overexpression, which

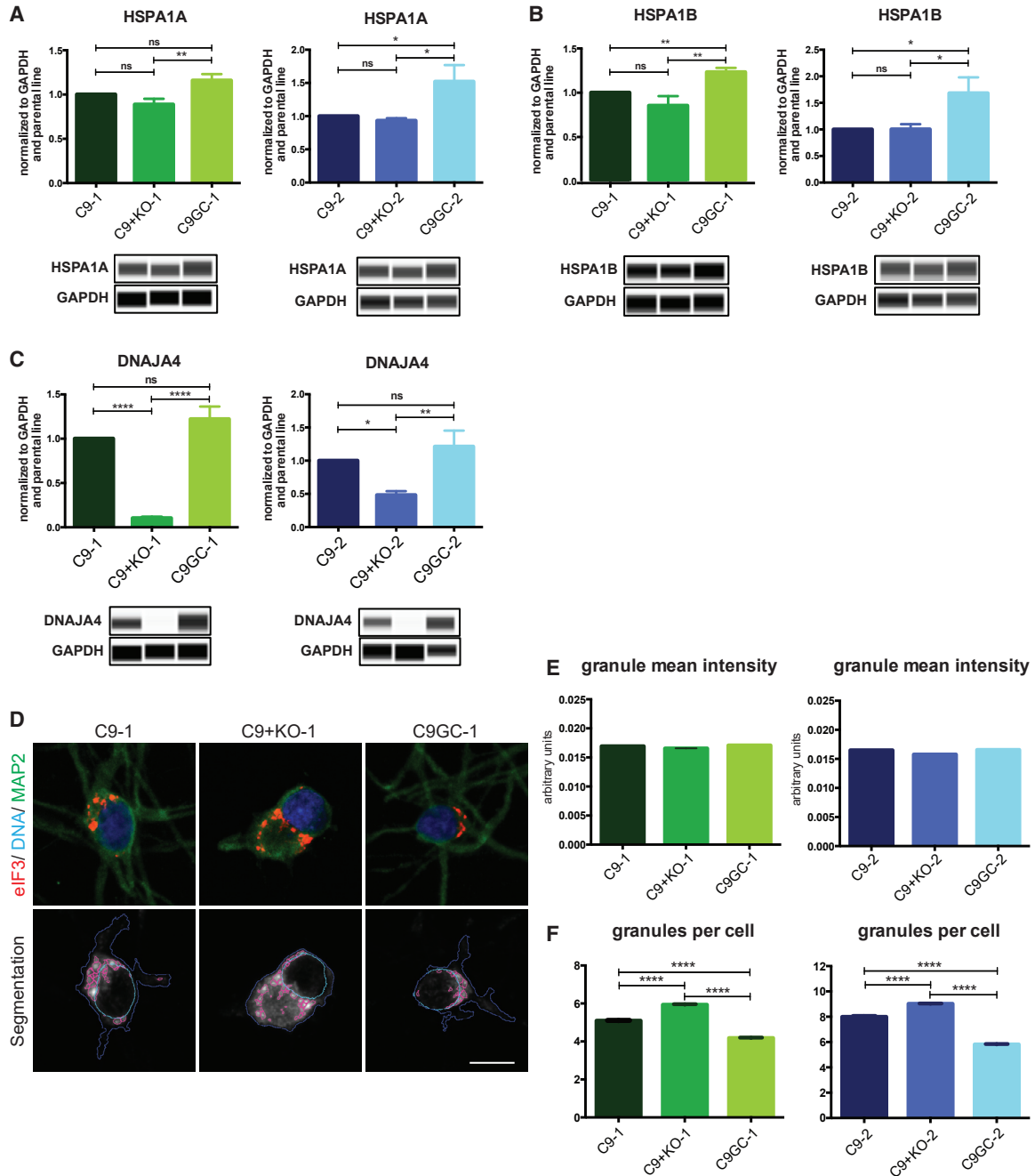


**Figure 6. HRE and Loss of C9ORF72 Reduce HSP40 and HSP70 Protein Levels and Alter SG Formation**

(A and B) Capillary electrophoresis showing that (A) HSPA1A and (B) HSPA1B are reduced in C9 MNs compared with C9GC controls. Levels were even further reduced in C9 + KO MNs.

(C) Capillary electrophoresis showing that DNAJA4 is reduced in C9 MNs compared with C9GC, and strikingly downregulated in C9 + KO MNs ( $n = 8$  biological replicates).

(D) Immunostaining of isogenic MNs with the indicated makers. Bottom panel shows segmentation of SGs, nuclei, and soma. Scale bar, 5  $\mu$ m.

(E) SG mean intensity was unaltered in MNs within the isogenic sets.

(F) Quantification revealed significantly higher number of SGs per cell in C9 MNs compared with C9GC, which was increased in C9 + KO neurons ( $n = 3$  biological replicates;  $>3,400$  cells and  $>12,000$  SGs).

All values are presented as mean  $\pm$  SEM. One-way ANOVA followed by Tukey's post-test for multiple comparisons was performed (\* $p < 0.05$ , \*\* $p < 0.01$ , \*\*\*\* $p < 0.0001$ , \*\*\*\* $p < 0.0001$ ).

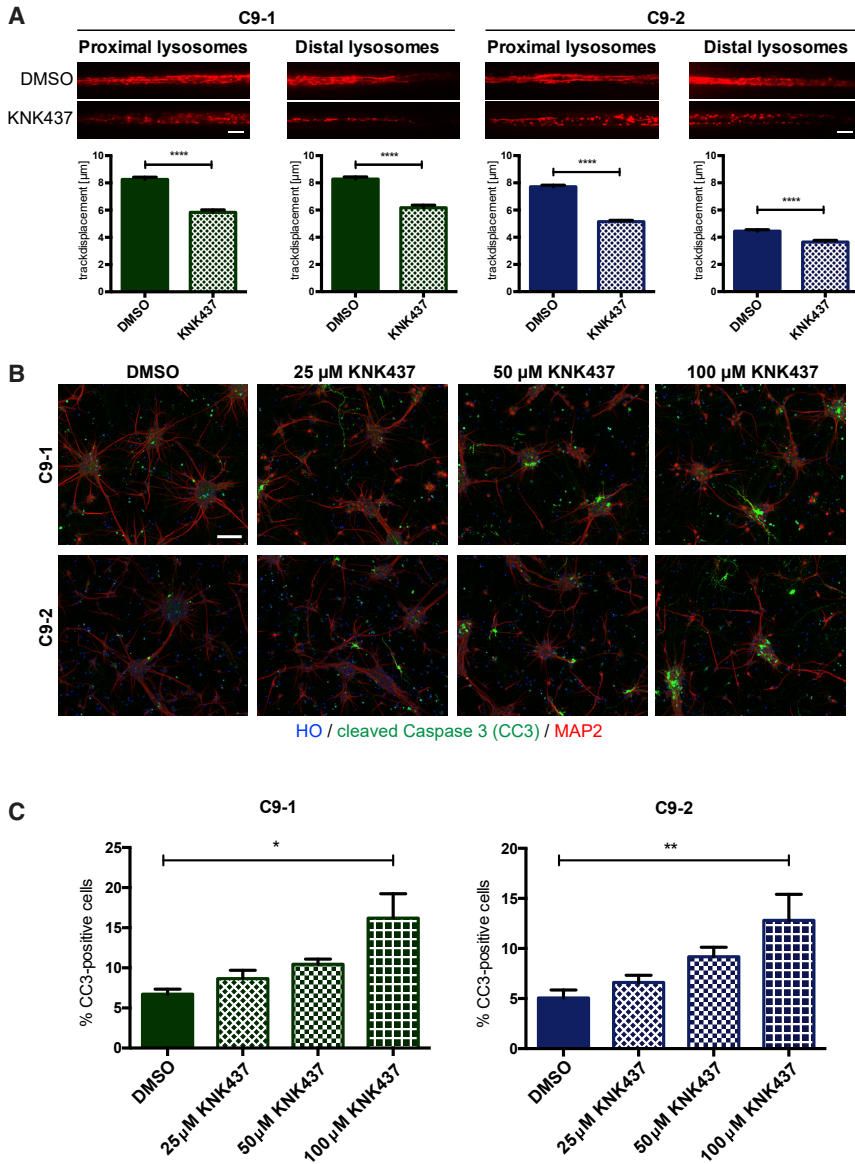


**Figure 7. HSP Inhibitor KNK437 Disrupts Axonal Trafficking and Induces Apoptosis in MNs with HRE**

(A) Maximum projection for C9-1 and C9-2 MNs treated with either DMSO or 200  $\mu\text{M}$  KNK437. Scale bars, 10  $\mu\text{m}$ . Quantification for lysosomal track displacement in  $\mu\text{m}$ . Mann-Whitney test was performed for statistical significance (\*\*\*\* $p < 0.0001$ ).  $N = 6$  biological replicates; >500 lysosomes were analyzed per cell line and per side for all experiments.

(B) Immunostaining for CC3 for C9-1 and C9-3 MNs treated with DMSO or the indicated concentration of KNK437. Scale bar, 50  $\mu\text{m}$ .

(C) Quantification shows percent CC3-positive cells.  $N = 4$  biological replicates. One-way ANOVA was used to calculate statistical significance (\* $p < 0.05$ , \*\* $p < 0.01$ ). See also Figure S7.

rely on promoters, such as the CMV-promoter, which usually results in RNA and protein levels that are higher than physiological levels. Moreover, we created an LOF model (wtKO) as well as a model for toxic GOF in which isogenic MNs with and without the HRE express similar levels of C9ORF72 protein. Our results show that axonal degeneration associated with HRE involves both GOF and LOF mechanisms by demonstrating that C9ORF72 KO exacerbated the effects of GOF caused by the HRE but the KO itself does not affect WT MNs. This exacerbation could have important implications for ALS therapeutics. Currently, antisense oligonucleotides (ASOs) are being developed to reduce the HRE-containing intronic RNA and downstream DPR protein levels (Jiang et al., 2016). Our results demon-

strate the importance that these ASOs avoid unintentional reduction of C9ORF72 protein levels to maintain physiological levels of C9ORF72.

To better understand the mechanism of pathogenesis, we performed transcriptome sequencing, which identified over 1,000 differentially expressed genes between C9 versus C9GC MNs, most of which were upregulated. Interestingly, we found that many of these genes were downregulated in C9 + KO versus C9 MNs. One possible explanation is that DPR proteins induced this differential gene expression, and DPR levels were lower in C9 + KO MNs. However, another explanation could be that these differentially expressed genes are part of a compensatory response used by MNs to maintain viability in the presence



of the HRE and that knocking out C9ORF72 protein may ablate this compensatory response, leading to more severe phenotypes. Both scenarios would explain why no phenotype was observed in wtKO MNs.

To our knowledge, our results are the first to report that decreased HSP activity could contribute to C9ORF72-ALS pathogenesis. Comparing our transcriptome data with those published by Selvaraj et al. (2018) showed that the HSP40 family member DNAJA4 was downregulated in both datasets, suggesting that HSPs play an important role in C9ORF72-ALS. We confirmed that DNAJA4 protein was misregulated, and showed that HSPA1A and HSPA1B were also misregulated. Consistent with this, transcriptome sequencing from the brain of C9ORF72-ALS patients show misregulation of HSPs (Prudencio et al., 2015). We showed that inhibiting HSPs significantly exacerbated C9ORF72-ALS phenotypes, including disrupting axonal transport and increasing apoptosis of MNs. Thus, it is possible that the most effective therapeutic strategy might be to combine ASOs, which aim at reducing DPR protein levels, together with the restoration of HSP levels, for example, using a gene therapy-based approach or a compound, such as arimoclomol, which is a co-inducer of HSPs currently being investigated in clinical trials for ALS that has shown promising results in mouse models (Benatar et al., 2018). However, the possibility has been raised that at least some HSPs might exacerbate ALS pathogenesis. For example, overexpression of HSF1, activating a heat shock response found in C9ORF72-ALS/FTLD patients, exacerbated eye degeneration in a *Drosophila* model (Mordes et al., 2018). Thus, further experiments are needed to test the role of specific HSPs in ALS phenotypes in human MNs.

One of the important functions of HSPs in human MNs is the regulation of SGs (Ganassi et al., 2016), which are crucial players in ALS pathogenesis. In addition, DPR proteins have already been shown to disrupt SG regulation (Lee et al., 2016), and, here, we demonstrate that HRE + C9ORF72 KO results in reduced levels of specific HSPs, exacerbating the SG phenotype. We found that the number of SGs per cell was increased in MNs with an HRE and even higher in MNs with HRE + C9ORF72 KO. Consistent with our data, a recent report demonstrated that removal of C9ORF72 led to increased accumulation of SGs in the cytoplasm and disrupted SG elimination by autophagy (Chitiprolu et al., 2018). This is of particular interest as it has been shown that disruption of microtubule transport proteins affects SG dynamics (Loschi et al., 2009). Because these same proteins also regulate axonal transport, it suggests that there is a general defect in microtubule-based transport in MNs with HRE in C9ORF72. Since SGs tend to accumulate misfolded proteins, this could indicate that MNs with HRE in C9ORF72 have defects in protein homeo-

stasis and that C9ORF72 KO exacerbates these effects, which is consistent with our observation that HSPs were downregulated.

One interesting point is the existence of variability in how human MNs respond to reduced C9ORF72 levels. At least one group found that reducing C9ORF72 levels in human MNs led to degeneration (Shi et al., 2018). Although this is a different assay than our assessment of axonal trafficking, the differences in the severity of the phenotypes are noticeable. We suggest that variations in the genetic background could explain the different observations. Unlike mutations in rarer ALS loci, such as *FUS* or *SOD1*, HRE in C9ORF72 show age-dependent penetrance and do not achieve full penetrance until a very advanced age (Majounie et al., 2012). Even more striking, members of a single family inheriting the same mutation can exhibit different diseases, namely ALS or frontotemporal dementia or, occasionally, a mixture (Simon-Sanchez et al., 2012). Thus, the genetic background and, perhaps, environmental agents, can significantly impact the phenotype of patients. For example, *ATXN2*, *TMEM106B*, and *SPT4* have already been shown to be critical modulators of C9ORF72 pathogenesis (van Blitterswijk et al., 2014). This implies that iPSCs could be combined with human genetics and gene editing to tease apart the influences of other loci on the phenotypes of human MNs with HRE in C9ORF72.

## EXPERIMENTAL PROCEDURES

A complete description of the methods can be found in the [Supplemental Information](#).

### iPSC Culture and MN Differentiation

iPSC generation and MN differentiation is described in [Supplemental Information](#).

### Immunocytochemical Staining

MNs were fixed for 20 min with 4% paraformaldehyde (EM Science) in PBS (Life Technologies). Permeabilization and blocking were achieved with 0.1% Triton X-(Sigma), 10% fetal calf serum (GE Healthcare) and 1% BSA (Roth) in PBS for 45 min and primary antibodies incubated overnight at 4°C. The cells were washed twice with 1% BSA in PBS and secondary antibodies were applied for 1 h at room temperature. The cells were washed twice with 1% Tween 20 (AppliChem) in PBS, then incubated with Hoechst for 5 min and washed with PBS. Imaging was performed using an inverted Apotome Zeiss Axio/Observer Z1 microscope (Zeiss) and analyzed using FIJI and Adobe Photoshop. The following primary antibodies were used: chicken anti MAP2 1:10,000 (Abcam, ab92434), goat anti-eIF3 1:300 (Santa Cruz, sc-16377), goat anti-SOX2 1:300 (Santa Cruz, sc-17320), mouse anti-OCT4 1:300 (Santa Cruz, sc-5279), mouse anti-SMI32 1:1,000 (Covance, SMI-32P), mouse anti-SSEA4 1:300 (DSHB, MC-813-70), mouse anti-TUJ1 1:1,000 (Covance, MMS-435P-250), rabbit anti-CC3 1:500 (Cell Signaling, 9661S), rabbit anti-Islet1 1:1,500 (Abcam, ab20670),



rat anti-poly-GP 18 1:1,000 (kindly provided by Dieter Edbauer). The following secondary antibodies were diluted 1:1,000 (all Invitrogen): fluorescein isothiocyanate donkey anti-chicken (SA1-72000), Alexa Fluor 647 donkey anti-goat (A-21447), Alexa Fluor 488 donkey anti-mouse (A-21202), Alexa Fluor 568 donkey anti-mouse (A10037), Alexa Fluor 647 donkey anti-mouse (A-31571), Alexa Fluor 488 donkey anti-rabbit (A-21206), Alexa Fluor 568 donkey anti-rabbit (A10042), Alexa Fluor 647 donkey anti-rabbit (A-31573), Alexa Fluor 568 goat anti-rat (A-11077), Hoechst 33342 (H1399).

### Live-Cell Imaging and High Content Imaging

The technique has already been described (Pal et al., 2018). Microfluidic chambers (Xona Microfluidics) were used with glass bottom dishes coated with laminin. MNs (150,000) were seeded, and N2B27 with BDNF and GDNF was applied to the distal side. At day 14, lysosomes were labeled using LysoTracker (Thermo Fischer Scientific) and imaged using a Leica DMI6000 microscope in an incubator chamber.

### Capillary Gel Electrophoresis

MNs were lysed in a 4% SDS buffer supplemented with 50 mM Tris base (Roth), protease- and phosphatase inhibitor (Roche), and protein concentration determined using a bicinchoninic acid assay (Thermo Fisher Scientific). Protein expression levels were measured with capillary electrophoresis using a 12-230 separation module from ProteinSimple Wes (ProteinSimple, Bio-Techne). Utilized primary antibodies included: rabbit anti GAPDH 1:1,000 (Cell Signaling, 2118S), rabbit anti-DNAJA4 1:40 (Atlas Antibodies, HPA041790), rabbit anti-HSPA1A 1:1,000 (BIOZOL, GTX111088), rabbit anti-HSPA1B 1:100 (BIOZOL, GTX106148), rabbit anti-C9ORF72 1:30 (Sigma, HPA023873).

### SUPPLEMENTAL INFORMATION

Supplemental Information can be found online at <https://doi.org/10.1016/j.stemcr.2020.01.010>.

### AUTHOR CONTRIBUTIONS

M.A.-R., J.L.S., and F.W. designed the research. M.A.-R. performed gene editing, disease modeling, and phenotypic assays. F.W., S.P., S.Staeger, and N.K. performed electrophysiology experiments and qRT-PCR. A.P. and A.H. helped with axonal trafficking analysis. C.L. and D.E. performed ELISA assays and provided poly-GP antibody. W.J. and T.R. performed Southern blot, repeat-primed PCR and amplicon length PCR. M.B. and A.J. conducted high content imaging and analysis. S.Stefanov helped with transcriptome analysis. M.A.-R. and J.L.S. wrote the paper, which was critically revised by all authors.

### ACKNOWLEDGMENTS

This work was financed by DFG Research Center (DFG FZT 111) and Cluster of Excellence (DFG EXC 168). The Sternecker lab is supported by the European Union's Horizon 2020 research and innovation program (643417) and the Bundesministerium für Bildung und Forschung (01ED1601B). This is an EU Joint Program – Neurodegenerative Disease Research (JPND) project. The project

is supported by the following funding organizations under the aegis of JPND—[www.jpnd.eu](http://www.jpnd.eu): Germany, Bundesministerium für Bildung und Forschung; Israel, Ministry of Health, Italy, Ministero dell'Istruzione, dell'Università e della Ricerca; Sweden, Swedish Research Council; and Switzerland, Swiss National Science Foundation. This project was additionally funded by the Robert Packard Center for ALS Research. F.W., S.P., and N.K. were supported by a grant of the Petermax-Müller-Stiftung (Hannover, Germany). This work was supported in part by the NOMIS Foundation (to D.E. and A.H.), the Helmholtz Virtual Institute “RNA dysmetabolism in ALS and FTD (VH-VI-510)” (to A.H.), BIOCREA GMBH (to A.H.), an unrestricted grant by the family of a deceased ALS patient via the Stiftung zur Förderung der Hochschulmedizin in Dresden (to A.H.) and by the Hermann und Lilly Schilling-Stiftung für medizinische Forschung im Stifterverband (to A.H.). We thank Prof. J. Rothstein and A.H. for providing patient-specific iPSCs. We thank G. Jurado Jiménez and S. Gholamhosseinian for their support as student assistants. We thank T. Levin for editing the manuscript. This work was additionally supported by the CRTD Light Microscopy facility as well as the next-generation sequencing facility, in particular, M. Lesche and A. Petzold.

Received: February 18, 2019

Revised: January 18, 2020

Accepted: January 21, 2020

Published: February 20, 2020

### REFERENCES

- Benatar, M., Wu, J., Andersen, P.M., Atassi, N., David, W., Cudkowicz, M., and Schoenfeld, D. (2018). Randomized, double-blind, placebo-controlled trial of arimoclochol in rapidly progressive SOD1 ALS. *Neurology* 90, e565–e574.
- Chew, J., Gendron, T.F., Prudencio, M., Sasaguri, H., Zhang, Y.J., Castanedes-Casey, M., Lee, C.W., Jansen-West, K., Kurti, A., Murray, M.E., et al. (2015). C9ORF72 repeat expansions in mice cause TDP-43 pathology, neuronal loss, and behavioral deficits. *Science* 348, 1151–1154.
- Chitiprolu, M., Jagow, C., Tremblay, V., Bondy-Chorney, E., Paris, G., Savard, A., Palidwor, G., Barry, F.A., Zinman, L., Keith, J., et al. (2018). A complex of C9ORF72 and p62 uses arginine methylation to eliminate stress granules by autophagy. *Nat. Commun.* 9, 2794.
- Ciura, S., Lattante, S., Le Ber, I., Latouche, M., Tostivint, H., Brice, A., and Kabashi, E. (2013). Loss of function of C9orf72 causes motor deficits in a zebrafish model of amyotrophic lateral sclerosis. *Ann. Neurol.* 74, 180–187.
- Devlin, A.C., Burr, K., Borooah, S., Foster, J.D., Cleary, E.M., Geti, I., Vallier, L., Shaw, C.E., Chandran, S., and Miles, G.B. (2015). Human iPSC-derived motoneurons harbouring TARDBP or C9ORF72 ALS mutations are dysfunctional despite maintaining viability. *Nat. Commun.* 6, 5999.
- Frick, P., Sellier, C., Mackenzie, I.R.A., Cheng, C.-Y., Tahraoui-Bories, J., Martinat, C., Pasterkamp, R.J., Prudlo, J., Edbauer, D., Oulad-Abdelghani, M., et al. (2018). Novel antibodies reveal presynaptic localization of C9orf72 protein and reduced protein levels in C9orf72 mutation carriers. *Acta Neuropathol. Commun.* 6, 72.



- Ganassi, M., Mateju, D., Bigi, I., Mediani, L., Poser, I., Lee, H.O., Seuguin, S.J., Morelli, F.F., Vinet, J., Leo, G., et al. (2016). A surveillance function of the HSPB8-BAG3-HSP70 chaperone complex ensures stress granule integrity and dynamism. *Mol. Cell* 63, 796–810.
- Gijselink, I., Van Langenhove, T., van der Zee, J., Slegers, K., Philtjens, S., Kleinberger, G., Janssens, J., Bettens, K., Van Cauwenberghe, C., Pereson, S., et al. (2012). A C9orf72 promoter repeat expansion in a Flanders-Belgian cohort with disorders of the frontotemporal lobar degeneration-amyotrophic lateral sclerosis spectrum: a gene identification study. *Lancet Neurol.* 11, 54–65.
- Hruscha, A., Krawitz, P., Rechenberg, A., Heinrich, V., Hecht, J., Haass, C., and Schmid, B. (2013). Efficient CRISPR/Cas9 genome editing with low off-target effects in zebrafish. *Development* 140, 4982–4987.
- Jiang, J., Zhu, Q., Gendron, T.F., Saberi, S., McAlonis-Downes, M., Seelman, A., Stauffer, J.E., Jafar-nejad, P., Drenner, K., Schulte, D., et al. (2016). Gain of toxicity from ALS/FTD-Linked repeat expansions in C9ORF72 is alleviated by antisense oligonucleotides targeting GGGGCC-containing RNAs. *Neuron* 90, 535–550.
- Lee, K.-H., Zhang, P., Kim, H.J., Mitrea, D.M., Sarkar, M., Freibaum, B.D., Cika, J., Coughlin, M., Messing, J., Molliex, A., et al. (2016). C9orf72 dipeptide repeats impair the assembly, dynamics, and function of membrane-less organelles. *Cell* 167, 774–788.e17.
- Li, Y.R., King, O.D., Shorter, J., and Gitler, A.D. (2013). Stress granules as crucibles of ALS pathogenesis. *J. Cell Biol.* 201, 361–372.
- Loschi, M., Leishman, C.C., Berardone, N., and Boccaccio, G.L. (2009). Dynein and kinesin regulate stress-granule and P-body dynamics. *J. Cell Sci.* 122, 3973–3982.
- Majounie, E., Renton, A.E., Mok, K., Dopper, E.G.P., Waite, A., Rollinson, S., Chiò, A., Restagno, G., Nicolaou, N., Simon-Sanchez, J., et al. (2012). Frequency of the C9orf72 hexanucleotide repeat expansion in patients with amyotrophic lateral sclerosis and frontotemporal dementia: a cross-sectional study. *Lancet Neurol.* 11, 323–330.
- Mordes, D.A., Prudencio, M., Goodman, L.D., Klim, J.R., Moccia, R., Limone, F., Pietilainen, O., Chowdhary, K., Dickson, D.W., Rademakers, R., et al. (2018). Dipeptide repeat proteins activate a heat shock response found in C9ORF72-ALS/FTLD patients. *Acta Neuropathol. Commun.* 6, 55.
- Naujock, M., Stanslowsky, N., Bufler, S., Naumann, M., Reinhardt, P., Sternecker, J., Kefalakes, E., Kassebaum, C., Bursch, F., Lojewski, X., et al. (2016). 4-Aminopyridine induced activity rescues hypoexcitable motor neurons from amyotrophic lateral sclerosis patient-derived induced pluripotent stem cells. *Stem Cells* 34, 1563–1575.
- Naumann, M., Pal, A., Goswami, A., Lojewski, X., Japtok, J., Vehlow, A., Naujock, M., Günther, R., Jin, M., Stanslowsky, N., et al. (2018). Impaired DNA damage response signaling by FUS-NLS mutations leads to neurodegeneration and FUS aggregate formation. *Nat. Commun.* 9, 335.
- Niblock, M., Smith, B.N., Lee, Y.B., Sardone, V., Topp, S., Troakes, C., Al-Sarraj, S., Leblond, C.S., Dion, P.A., Rouleau, G.A., et al. (2016). Retention of hexanucleotide repeat-containing intron in C9orf72 mRNA: implications for the pathogenesis of ALS/FTD. *Acta Neuropathol. Commun.* 4, 18.
- Nicolas, A., Kenna, K.P., Renton, A.E., Ticozzi, N., Faghri, F., Chia, R., Dominov, J.A., Kenna, B.J., Nalls, M.A., Keagle, P., et al. (2018). Genome-wide analyses identify KIF5A as a novel ALS gene. *Neuron* 97, 1268–1283.e6.
- Pal, A., Glass, H., Naumann, M., Kreiter, N., Japtok, J., Sczech, R., and Hermann, A. (2018). High content organelle trafficking enables disease state profiling as powerful tool for disease modelling. *Sci. Data* 5, 180241.
- Parone, P.A., Da Cruz, S., Han, J.S., McAlonis-Downes, M., Vetto, A.P., Lee, S.K., Tseng, E., and Cleveland, D.W. (2013). Enhancing mitochondrial calcium buffering capacity reduces aggregation of misfolded SOD1 and motor neuron cell death without extending survival in mouse models of inherited amyotrophic lateral sclerosis. *J. Neurosci.* 33, 4657–4671.
- Prudencio, M., Belzil, V.V., Batra, R., Ross, C.A., Gendron, T.F., Pregent, L.J., Murray, M.E., Overstreet, K.K., Piazza-Johnston, A.E., Desaro, P., et al. (2015). Distinct brain transcriptome profiles in C9orf72-associated and sporadic ALS. *Nat. Neurosci.* 18, 1175–1182.
- Puls, I., Jonnakuty, C., LaMonte, B.H., Holzbaur, E.L.F., Tokito, M., Mann, E., Floeter, M.K., Bidus, K., Drayna, D., Oh, S.J., et al. (2003). Mutant dynactin in motor neuron disease. *Nat. Genet.* 33, 455–456.
- Sareen, D., O'Rourke, J.G., Meera, P., Muhammad, A.K.M.G., Grant, S., Simpkinson, M., Bell, S., Carmona, S., Ornelas, L., Sahabian, A., et al. (2013). Targeting RNA foci in iPSC-derived motor neurons from ALS patients with a C9ORF72 repeat expansion. *Sci. Translational Med.* 5, 208ra149.
- Selvaraj, B.T., Livesey, M.R., Zhao, C., Gregory, J.M., James, O.T., Cleary, E.M., Chouhan, A.K., Gane, A.B., Perkins, E.M., Dando, O., et al. (2018). C9ORF72 repeat expansion causes vulnerability of motor neurons to Ca(2+)-permeable AMPA receptor-mediated excitotoxicity. *Nat. Commun.* 9, 347.
- Shi, Y., Lin, S., Staats, K.A., Li, Y., Chang, W.-H., Hung, S.-T., Hendricks, E., Linares, G.R., Wang, Y., Son, E.Y., et al. (2018). Haploinsufficiency leads to neurodegeneration in C9ORF72 ALS/FTD human induced motor neurons. *Nat. Med.* 24, 313–325.
- Simon-Sanchez, J., Dopper, E.G., Cohn-Hokke, P.E., Hukema, R.K., Nicolaou, N., Seelaar, H., de Graaf, J.R., de Koning, I., van Schoor, N.M., Deeg, D.J., et al. (2012). The clinical and pathological phenotype of C9ORF72 hexanucleotide repeat expansions. *Brain* 135, 723–735.
- Tabet, R., Schaeffer, L., Freyermuth, F., Jambau, M., Workman, M., Lee, C.-Z., Lin, C.-C., Jiang, J., Jansen-West, K., Abou-Hamdan, H., et al. (2018). CUG initiation and frameshifting enable production of dipeptide repeat proteins from ALS/FTD C9ORF72 transcripts. *Nat. Commun.* 9, 152.
- van Blitterswijk, M., Mullen, B., Heckman, M.G., Baker, M.C., DeJesus-Hernandez, M., Brown, P.H., Murray, M.E., Hsiung, G.Y., Stewart, H., Karydas, A.M., et al. (2014). Ataxin-2 as potential disease modifier in C9ORF72 expansion carriers. *Neurobiol. Aging* 35, 2421.e13–2421.e17.
- Wainger, B.J., Kiskinis, E., Mellin, C., Wiskow, O., Han, S.S., Sandoe, J., Perez, N.P., Williams, L.A., Lee, S., Boulting, G., et al. (2014). Intrinsic membrane hyperexcitability of



amyotrophic lateral sclerosis patient-derived motor neurons. *Cell Rep.* 7, 1–11.

Waite, A.J., Baumer, D., East, S., Neal, J., Morris, H.R., Ansorge, O., and Blake, D.J. (2014). Reduced C9orf72 protein levels in frontal cortex of amyotrophic lateral sclerosis and frontotemporal degeneration brain with the C9ORF72 hexanucleotide repeat expansion. *Neurobiol. Aging* 35, 1779.e5–1779.e13.

Yokota, S., Kitahara, M., and Nagata, K. (2000). Benzylidene lactam compound, KNK437, a novel inhibitor of acquisition of thermotolerance and heat shock protein induction in human colon carcinoma cells. *Cancer Res.* 60, 2942–2948.

Zhang, Z., Almeida, S., Lu, Y., Nishimura, A.L., Peng, L., Sun, D., Wu, B., Karydas, A.M., Tartaglia, M.C., Fong, J.C., et al. (2013). Downregulation of microRNA-9 in iPSC-derived neurons of FTD/ALS patients with TDP-43 mutations. *PLoS One* 8, e76055.



**Supplemental Information**

**Knocking out C9ORF72 Exacerbates Axonal Trafficking Defects Associated with Hexanucleotide Repeat Expansion and Reduces Levels of Heat Shock Proteins**

**Masin Abo-Rady, Norman Kalmbach, Arun Pal, Carina Schludi, Antje Janosch, Tanja Richter, Petra Freitag, Marc Bickle, Anne-Karin Kahlert, Susanne Petri, Stefan Stefanov, Hannes Glass, Selma Staeger, Walter Just, Rajat Bhatnagar, Dieter Edbauer, Andreas Hermann, Florian Wegner, and Jared L. Sternecker**

## **Inventory of Supplemental Information**

### **1. Supplemental Figures**

- **Supplemental Figure S1.** Validation of gene editing. Related to Figure 1.
- **Supplemental Figure S2.** Quantitative RT-PCR analysis for *C9ORF72*.  
Related to Figure 1.
- **Supplemental Figure S3.** Karyotype and expression of pluripotency markers by gene edited iPSC lines. Related to Figure 1.
- **Supplemental Figure S4.** Characterization of iPSC-derived MNs. Related to Figure 2.
- **Supplemental Figure S5.** Eigengene and neuronal subtype marker analysis.  
Related to Figure 2.
- **Supplemental Figure S6.** Supplemental transcriptome analysis. Related to Figure 3.
- **Supplemental Figure S7.** RNAseq reads mapping to *C9ORF72* and directionality of axonal transport with KNK-437. Related to Figure 7.

### **2. Supplemental Experimental Procedures**

### **3. References**

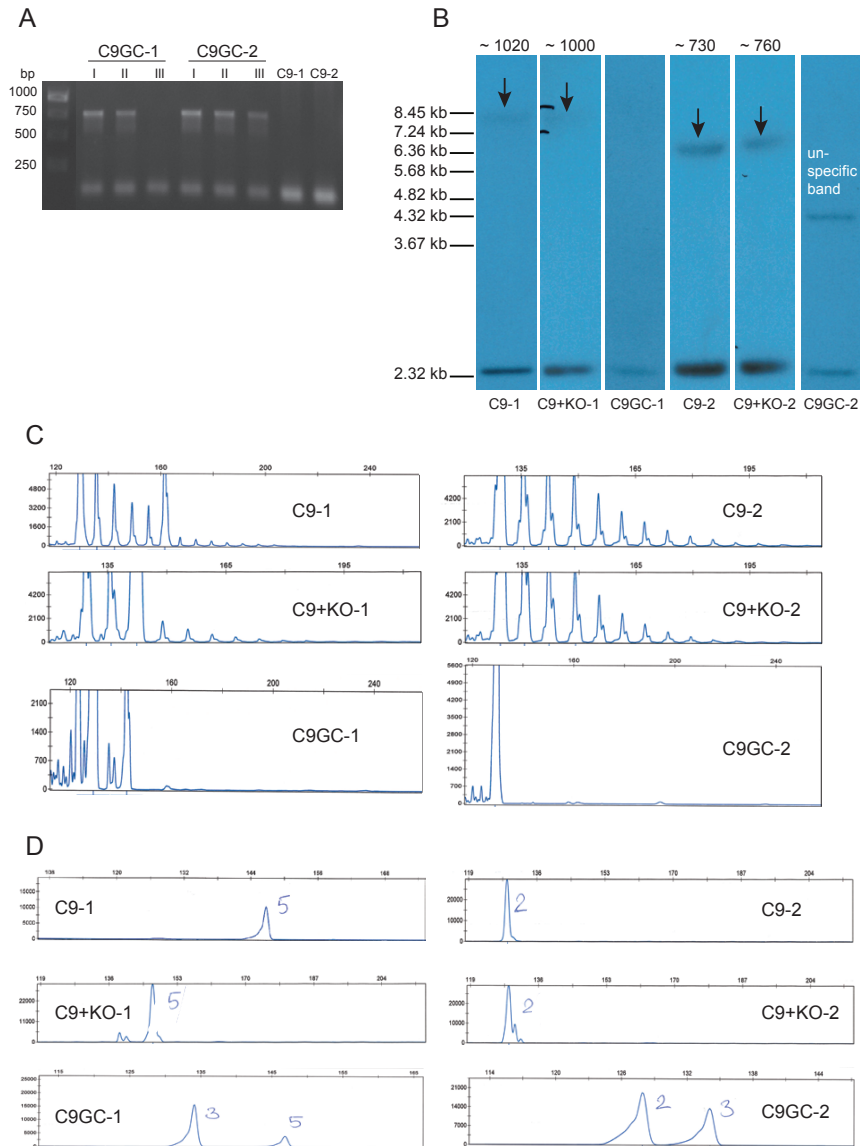
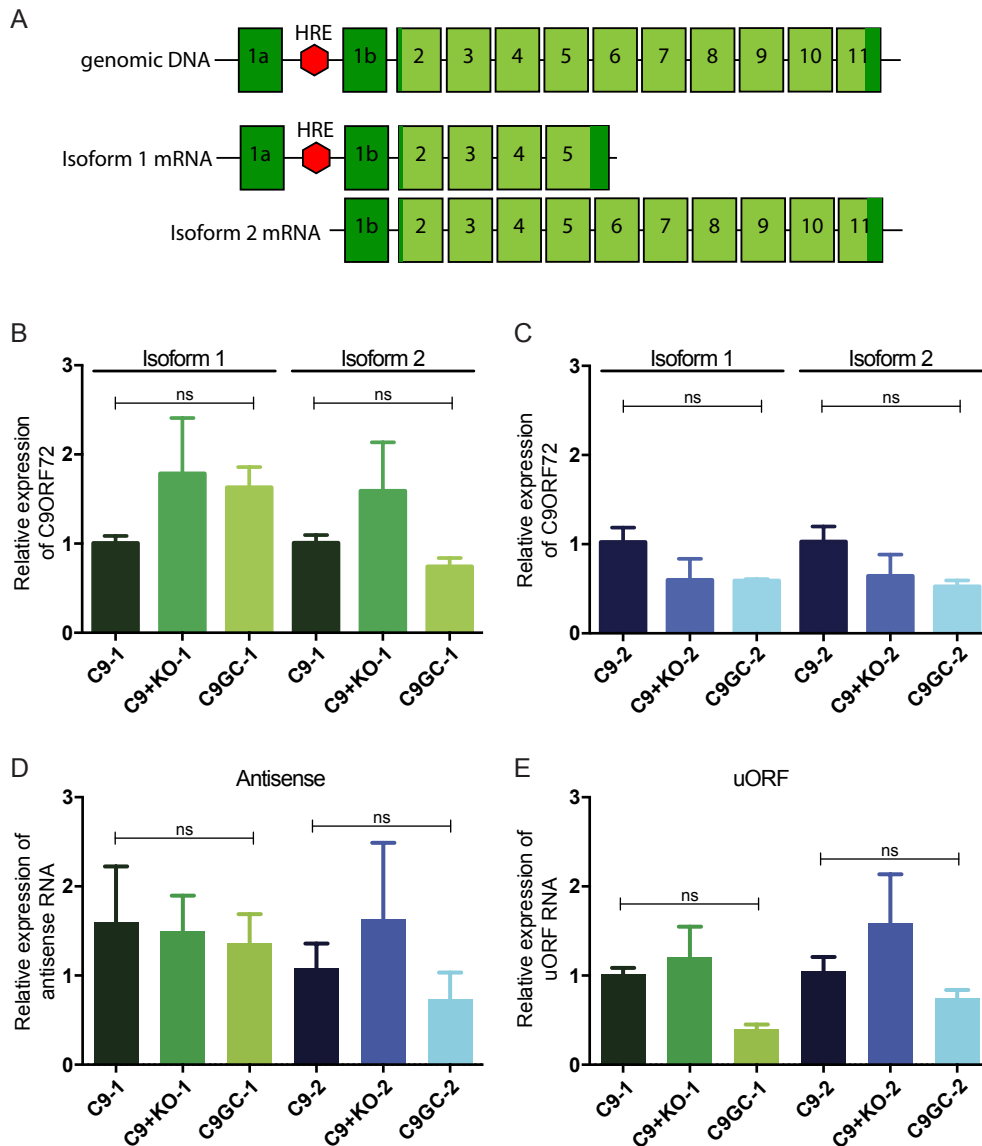


**Figure S1. Validation of gene editing. Related to Figure 1.** (A) PCR showing successful targeting of C9GC iPSC lines. (B) Southern blot confirmed absence of HRE in C9GC lines and HRE size of ~1000 G<sub>4</sub>C<sub>2</sub> repeats in C9-1 and C9+KO-1 and ~750 repeats in C9-2 and C9+KO-2. (C) Repeat-primed PCR confirmed presence of HRE in *C9ORF72* and C9+KO cells (ladder pattern) and absence in gene corrected lines. (D) Amplicon length PCR determined exact G<sub>4</sub>C<sub>2</sub> repeat size on alleles without HRE.



**Supplemental Figure S2. Quantitative RT-PCR analysis for *C9ORF72*. Related to Figure 1.** (A) Diagram illustrating *C9ORF72* isoforms analyzed. (B) Relative expression level of isoforms 1 and 2 using isogenic MNs from C9-1, C9+KO1, and C9GC-1. (C) Relative expression level of isoforms 1 and 2 using isogenic MNs from C9-2, C9+KO2, and C9GC-2. (D) Relative expression level of antisense *C9ORF72* using iPSC-derived MNs. (E) Relative expression levels of the open reading frame upstream of *C9ORF72* (uORF) using iPSC-derived MNs. All data represent means  $\pm$  SEM (n=3-5 biological replicates). For the quantification of target gene expression the threshold cycle (Ct) values of the targets were normalized against that of the

endogenous references ACTB, HPRT, TBP, and GAPDH. One-Way ANOVA was performed and showed no significant changes in expression levels. Bars indicate SEM.

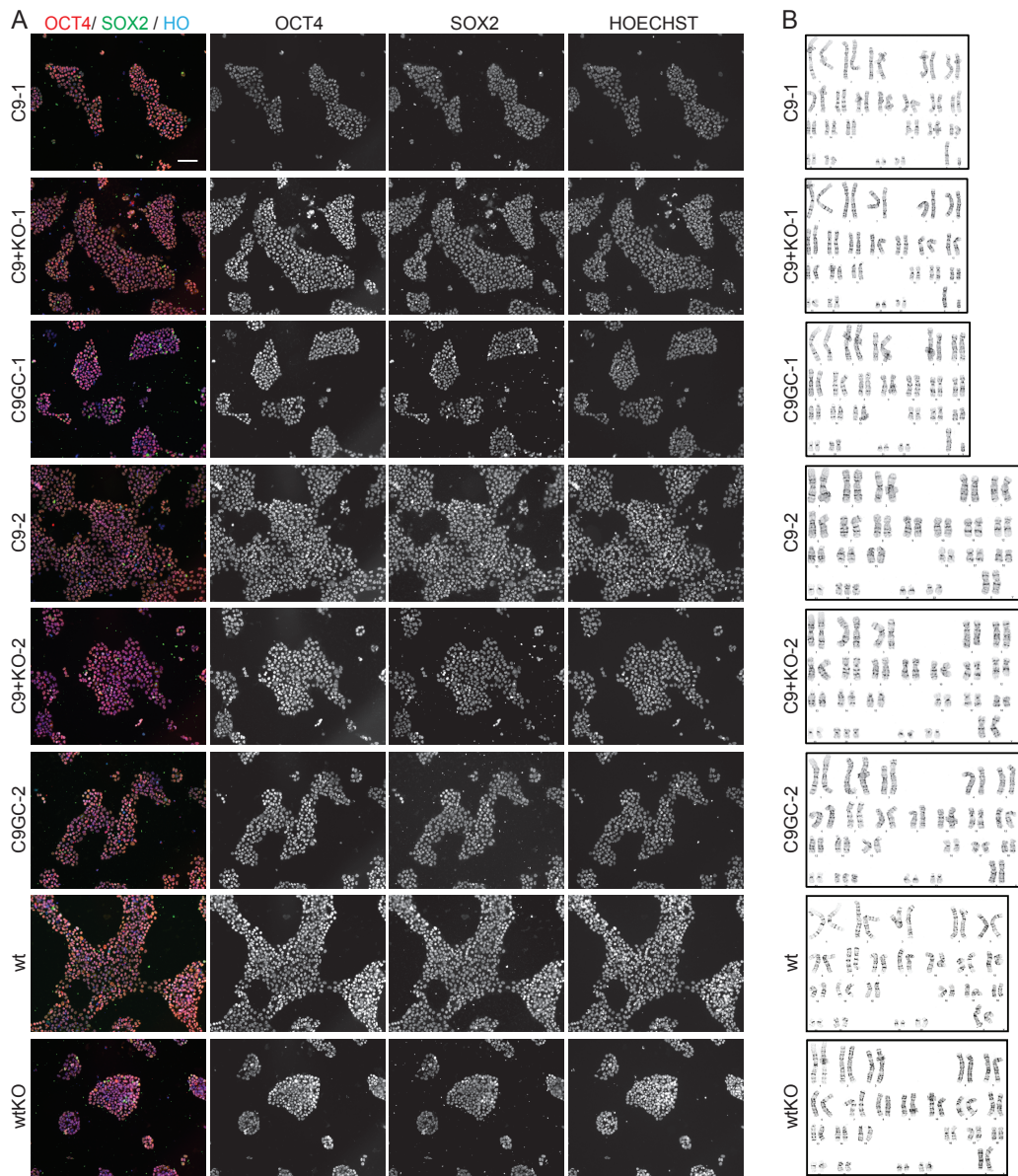


**Figure S3. Karyotype and expression of pluripotency markers by gene edited iPSC lines. Related to Figure 1. (A)** Immunostaining of the indicated iPSCs for the indicated markers. Scale bar: 100  $\mu$ m. **(B)** Karyogram of the indicated cell lines.

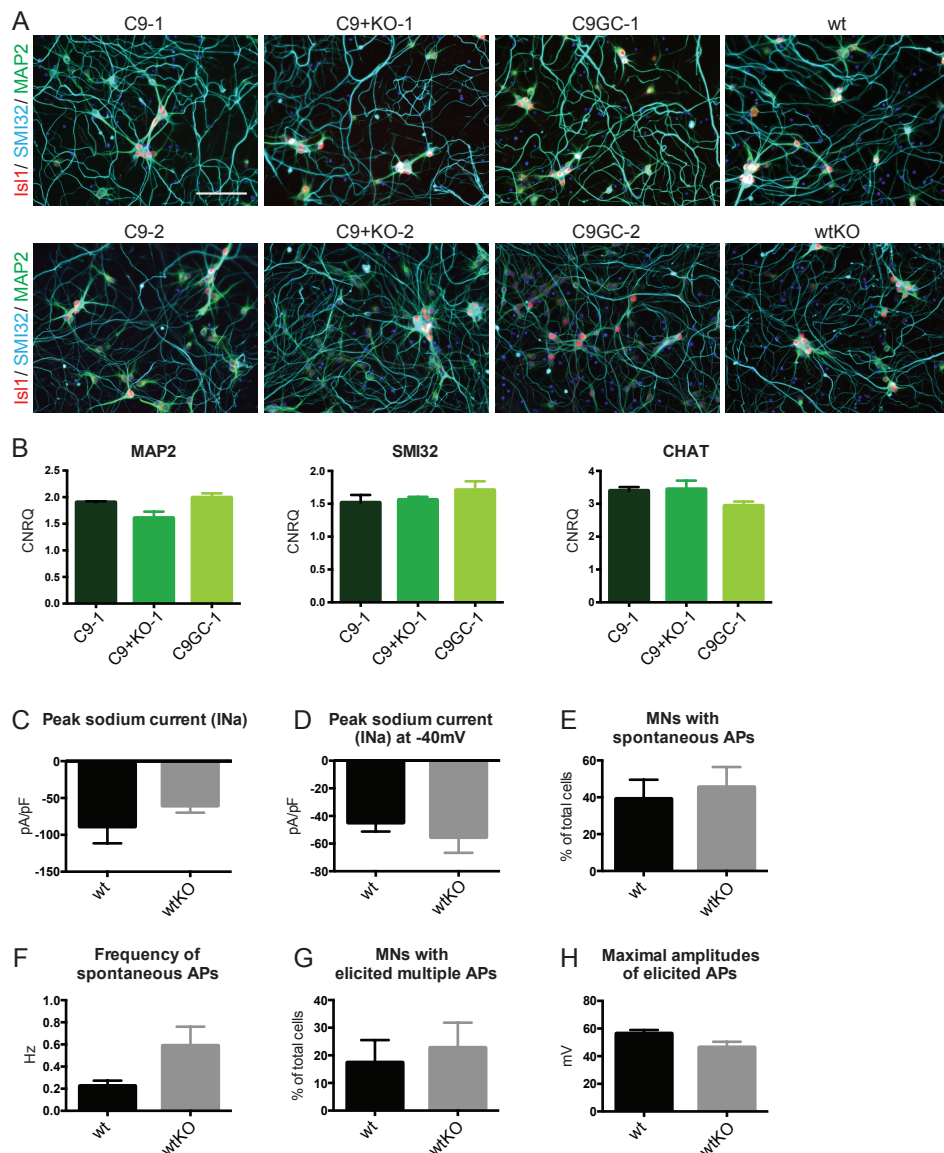
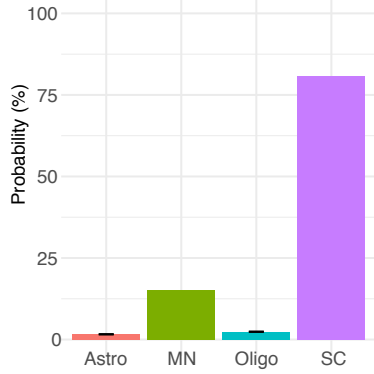


**Figure S4. Characterization of iPSC-derived MNs. Related to Figure 2.** (A) Immunostaining of differentiated MNs for the indicated MN markers. Scale bar: 100  $\mu$ m. (B) qRT-PCR confirmed that MAP2 and MN markers SMI32 and CHAT are expressed at comparable levels across the lines (represented within isogenic set 1; n=3 biological replicates). Calibrated normalized relative quantity (CNRQ) of marker expression was calculated for differentiated MNs relative to progenitor cells. (E-H) Whole-cell patch-clamp recordings of voltage-gated sodium channels (INa) and action potentials (APs) confirmed electrophysiological activity in wt and wtKO MNs. No

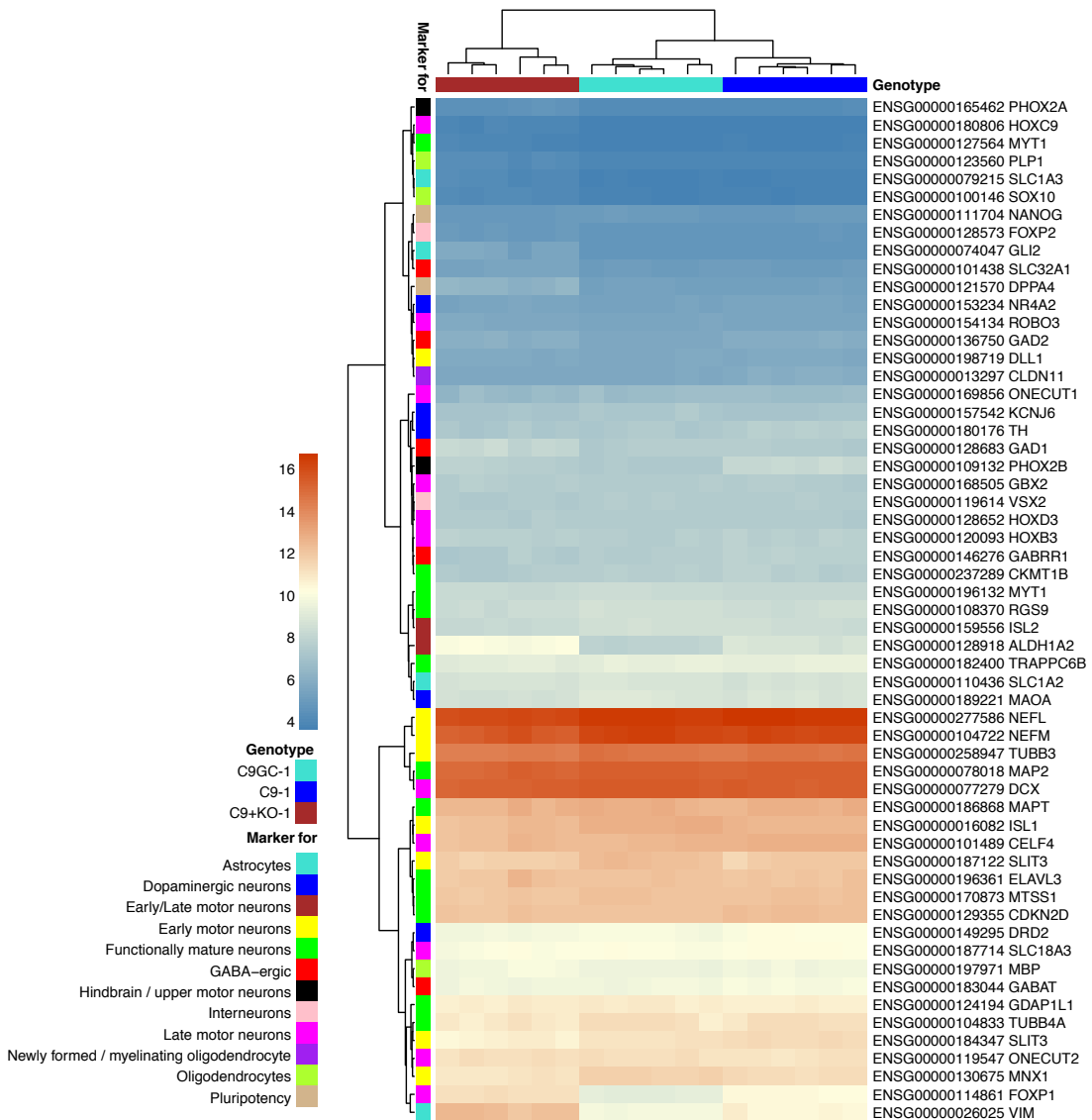
significant differences in the tested properties could be found between these isogenic cells. A minimum of  $n=22$  cells was measured per line.



### A Eigengene Classification

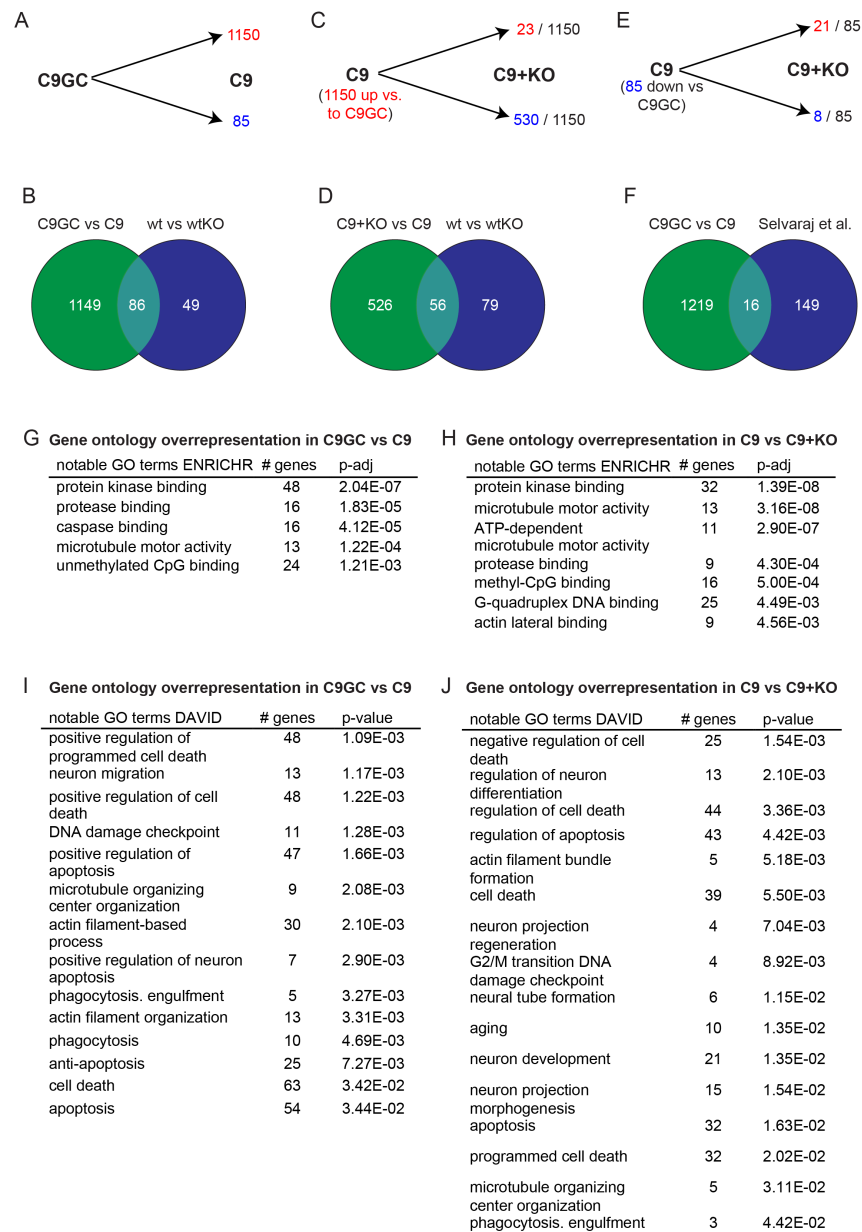


### B Subtype Marker Analysis



### Supplemental Figure S5. Eigengene and neuronal subtype marker analysis.

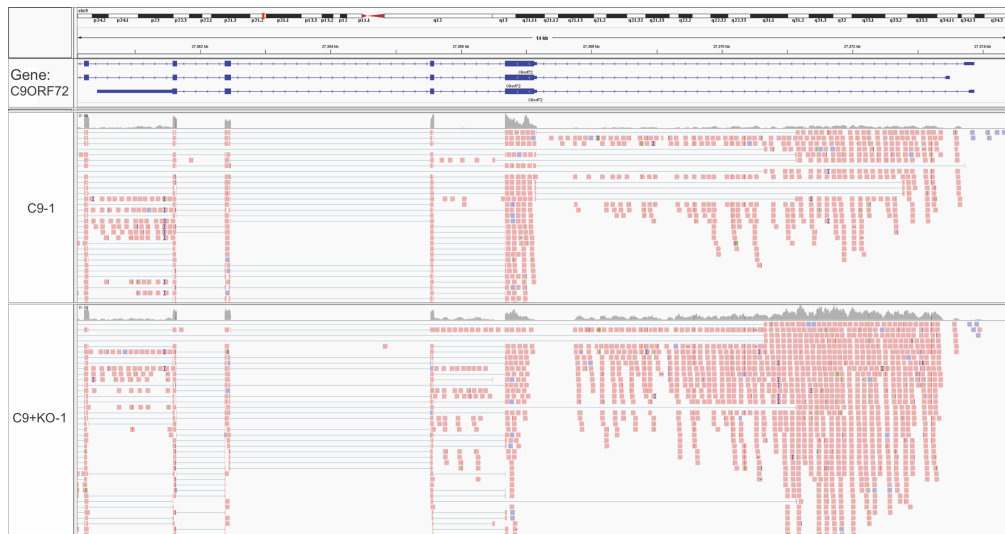
Related to Figure 2. (A) Eigengene classification identifies the cells in iPSC-derived MN cultures with whole spinal cord with 80% probability. (B) Heat map showing expression levels of the indicated neuronal subtype markers.



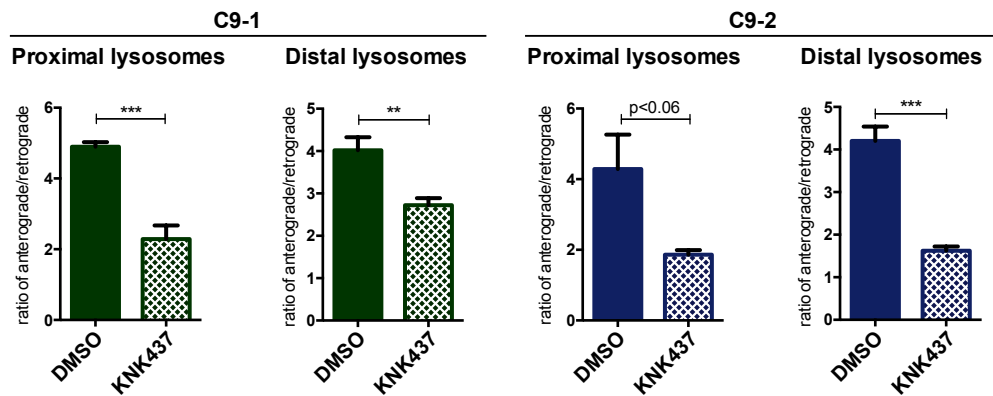
**Figure S6. Supplemental transcriptome analysis. Related to Figure 3.** (A) Direction of change is indicated for genes differentially expressed between C9GC vs C9. (B) Venn diagram showing overlap between C9GC vs C9 and wt vs wtKO. (C) Analysis of the 1150 genes that were upregulated in C9 compared with C9GC. Here, we show how many of these 1150 are up vs down regulated in C9+KO compared with C9. (D) Venn diagram showing overlap between C9+KO vs C9 and wt vs wtKO. (E) Analysis of the 85 genes that were downregulated in C9 compared with C9GC. Here, we show how many of these 85 are up vs down regulated in C9+KO compared with C9. (F) Venn

diagram showing overlap between C9GC vs C9 and the differentially expressed genes reported by Selvaraj et al. (Selvaraj et al., 2018). (G) Overrepresented GO terms in C9GC vs C9 using ENRICH analysis tool. (H) Overrepresented GO terms in C9 vs C9+KO using ENRICH analysis tool. (I) Overrepresented GO terms in C9GC vs C9 using DAVID analysis tool. (J) Overrepresented GO terms in C9 vs C9+KO using DAVID analysis tool.

A



B



**Figure S7. RNaseq reads mapping to *C9ORF72* and directionality of axonal transport with KNK437. Related to Figure 5. (A) Three transcripts depicted in blue (direction from right to left). Data show that the HRE containing intron 1 is retained in C9+KO MNs, possibly due to alterations of the splice acceptor site. (B) Direction of lysosomal transport in C9-1 or C9-2 MNs treated with DMSO or 200  $\mu$ M KNK437. Mann-Whitney test was performed for statistical significance. N=6 biological replicates; >500 lysosomes were analyzed per cell line and per side for all experiments.**

## SUPPLEMENTAL EXPERIMENTAL PROCEDURES

### Gene targeting

For targeting *C9ORF72*, a double nickase CRISPR/Cas9n system was used to generate knock out (KO) of *C9ORF72* protein in wt and mutant background, as well as gene correction (GC) of the *C9ORF72* repeat expansion in 2 parental ALS patient-derived *C9ORF72* iPSC lines. To generate KO lines, two vectors were designed, one upstream of translational start site in exon 2 (called “C9KOus”) and one in the second half of exon 2 (called “C9KOin”). For producing GC lines, one vector was designed to cut the DNA upstream of the GGGGCC repeat expansion (called “C9GCus”) to enable a repair with a synthesized zeocin cassette containing donor vector (called “GCz”, ATG:biosynthetics). The CRISPR/Cas9n vectors were designed to create double strand breaks (DSB) at target sites T1 and T2. Two single guide RNAs (sgRNAs), “a” and “b”, were ligated in each vector with “a” binding the positive and “b” binding the negative DNA strand, resulting in a DSB with 5'-overhang as “a” binds upstream of “b”.

By manually screening the positive (+) DNA strand close to the target sequences, sgRNA were selected and designed under the following criteria and validated with the online tool <http://crispr.mit.edu/> :

- Target 1 is upstream of Target 2
- “a” : sequence CCN(N)19C or CCN(N)20C to create nick on + strand
- “b” : sequence G(N)19NGG or G(N)20NGG to create nick on – strand
- to achieve paired nicking 3'-C or 5'-G can be added, if needed
- 0-15 bp offset between targets

Each sgRNA is assembled from two complementary DNA oligonucleotides, forward (fw) and reverse (rev). To enable the ligation of the sgRNAs into the expression vector

pX335B\_hCas9\_2x\_long\_chimeric\_gRNA\_G2P (a kind gift from Dr. Boris Greber, Max Planck Institute for Molecular Biomedicine, Münster, Germany) the 5'-overhangs needed to be included in the sgRNAs. For the fw oligonucleotide, “a” received an AAC-overhang and “b” received an AAAC-overhang, whereas to the rev oligonucleotide in “a” and “b” a CACC-overhang was added. The final vector contained both sgRNAs and a GFP-T2K-puromycin cassette. The following sgRNAs were used:

| Oligonucleotides | Sequence (5' → 3')        |
|------------------|---------------------------|
| C9GC_usT1a       | caccgAGTAGTGGGGAGAGAGGGT  |
| C9GC_usT2a       | caccGCTCTCACAGTACTCGCTGA  |
| C9GC_usT1b       | aaacACCCTCTCTCCCCACTACTc  |
| C9GC_usT2b       | aacTCAGCGAGTACTGTGAGAGC   |
| C9KO_usT1a       | caccGGGGTCATACTGGATTAGAG  |
| C9KO_usT2a       | caccGATTACACTTATTTCTAGATA |
| C9KO_usT1b       | aaacCTCTAATCCAGTATGACCCC  |
| C9KO_usT2b       | aacTATCTAGAAATAAGTGTAATC  |
| C9KO_inT1a       | caccGCCCAAATGTGCCTTACTCT  |
| C9KO_inT2a       | caccGAACAGGTACTTCTCAGTGA  |
| C9KO_inT1b       | aaacAGAGTAAGGCACATTTGGGC  |
| C9KO_inT2b       | aacTCACTGAGAAGTACCTGTTC   |

Single guided RNAs were cloned into the CRISPR/Cas9n vector using BbsI and SapI to insert the first and the second guide, respectively, and ligated using a T4 Ligase (NEB). The produced plasmids were transformed in competent *E. coli* TOP10 cells and tested for successful cloning utilizing colony PCR, using the according “T1a” oligonucleotide as forward primer and pX335\_seq\_rev (GGAAAGTCCCTATTGGCGTT) as reverse primer. The resulting PCR fragment was run on a 1% agarose gel and sequenced for quality control.

### **iPSC culture and transfection**

All procedures were performed in accordance with the Helsinki convention and approved by the Ethical Committee of the Technische Universität Dresden

(EK45022009, EK393122012). Patients and controls gave their written informed consent prior to skin biopsy. iPSC generation has been described previously (Donnelly et al., 2013; Naumann et al., 2018; Sivadasan et al., 2016). Cells were cultured in TeSR-E8 medium (Stem cell Technologies) at 37°C and 5% CO<sub>2</sub> with daily media changes and regular passaging. For gene targeting, iPSCs were seeded in a density of 200,000 cell/well of a 6-well dish in medium supplemented with ROCK inhibitor. The next day, the medium was exchanged and 1 µg of each vector (for KO C9KO<sub>us</sub> + C9KO<sub>in</sub>, for GC C9GC<sub>us</sub> + GCz) was transfected using FuGENE®HD (Promega) according to manufacturer's instructions. After 24h cells were checked for GFP expression, medium was changed and selection was started with 0.6 – 0.8 µg/ml puromycin for two. After 3 days recovery cells were split and seeded in single cell density. In case of GC, cells were treated with 2 µg/ml zeocin (Zeo) for a minimum of 5 days. The colonies were cultured for 7-12 days and validated by genotyping PCRs using the following primers:

| Primer    | Sequence 5' → 3'      |
|-----------|-----------------------|
| gtGCz fw  | CGGAGCCAGTACACGACATC  |
| gtGCz rev | TGTGTCATCTCGGAGCTGTG  |
| gtKO fw   | CCTGGCTTCTGGTGGTTACC  |
| gtKO rev  | GCTCCCAAGAAGAATCCAGGG |

Successfully targeted clones were expanded and used for further testing, as well as derivation of MNPs and MN differentiation.

### **MN differentiation**

Human iPSCs were seeded on mouse embryonic fibroblasts and cultured in human ES medium supplemented with 5 ng/ml FGF2 and 2.5 ng/ml Activin A (ActA, eBioscience). At day 3, supplements were removed, cells detached with collagenase (Life Technologies) and neuronal induction initiated using hES medium supplemented with 200 µM ascorbic acid (AA, Sigma), 3 µM CHIR 99022 (Axon Medchem), 10 µM

SB431542 (Biomol), 5  $\mu$ M dorsomorphine (DM, Absource) and 5  $\mu$ M ROCK inhibitor (Y-27632, Abcam) resulting in the formation of embryoid bodies (EB). Medium was changed every other day and after 4 days changed to N2B27 medium - DMEM F12 medium 1:1 Neurobasal medium supplemented with N2 and B27 (all Thermo Fischer Scientific), penicillin, streptomycin, glutamine (MerckMillipore)- and supplemented with 200  $\mu$ M AA, 3  $\mu$ M CHIR, 0.5  $\mu$ M valporic acid (VPA, Biomol), 0.5  $\mu$ M purmorphamine (PMA, Santa Cruz Biotech), 0.5  $\mu$ M DM, 10 $\mu$ M SB431542 and 0.1  $\mu$ M retinoic acid (RA, Sigma). After 2 more days, EBs were transferred to a 12-well matrigel-covered (Corning) dish, dissociated, and grown in monolayer as motor neuron progenitors (MNPs). MNPs were kept in culture and split with accutase (Sigma). To induce differentiation, N2B27 medium was supplemented with 200  $\mu$ M AA, 3  $\mu$ M CHIR, 0.5 PMA, 1  $\mu$ M RA, 10 ng/ml BDNF and 20 ng/ml GDNF (both Peprotech). After 6 days, medium was changed to maturation medium consisting of N2B27 with 200  $\mu$ M AA, 10 ng/ml BDNF, and 20 ng/ml GDNF, 200  $\mu$ M dibutyl cyclic adenosine monophosphate (dbcAMP, Selleckchem), 1 ng/ml transforming growth factor  $\beta$ 3 (TGF $\beta$ 3, Peprotech) and 5  $\mu$ M DAPT (Biomol). Two days later, MNs in early maturation phase were re-seeded on the final plate formats. After one week, DAPT was removed from the medium and MNs were kept in culture for a total time of 2-3 weeks.

### **Karyotyping**

Half confluent iPSCs were treated for 4 h with 0.35  $\mu$ g/ml colcemid (Sigma) and subsequently incubated at 37°C in 75 mM KCl (Sigma) for 20 min. The cells were fixed with methanol and acetic acid (both Roth) (3:1) and the cell suspension was dropped onto glass slides. For G-banding a standard protocol was used (Jhanwar et al., 1994).



### **Repeat primed PCR and amplicon length PCR**

To verify the existence of the HRE in *C9ORF72* samples and the absence in the gene corrected lines, repeat primed PCR was performed as previously described (Güven et al., 2016). To determine the exact length of GGGGCC repeats in the gene corrected cell lines, amplicon length PCR was performed as described (Akimoto et al., 2014). The resulting PCR products were analyzed with a 3730 DNA Analyzer and the regarding Peak Scanner Software v1.0 (both Applied Biosystems).

### **Southern blotting**

Southern blotting was performed as described (Güven et al., 2016). Briefly, a total of 10 µg of gDNA was digested with XbaI and HindIII at 37°C for 3–5 hours and electrophoresed in 0.8% agarose gel. For size determination, DNA size standards λBstEII and 2.5 kb ladder were added. After electrophoresis, the coordinates of the size standards were transferred to a stripe of white paper for the subsequent analysis of the sample results. DNA was transferred to a positively charged nylon membrane. Following pre-hybridization in Church buffer at 71°C for 3 hours, hybridization was carried out at 71°C overnight. The blot was hybridized with a random primed-α<sup>32</sup>P-dCTP-labeled probe flanking the hexanucleotide repeat. The membranes were then washed in 1% sodium dodecyl sulphate (SDS) and 0.5 M Na-phosphate at 56–58°C. The membranes were exposed to X-ray films for 4 days at -70°C applying an intensifying screen. For measurement of the expanded alleles, the marker data (migration distance and size) from the paper stripes were transferred to semi-logarithmic graph paper. A regression curve was plotted by connecting all data points. The hybridization signals of the X-ray film were also transferred to the semi-logarithmic graph paper, pinpointing the size of the expanded (and normal) alleles.

## **Electrophysiology**

Whole-cell patch-clamp recordings of MNs were performed as described previously (Naujock et al., 2016) during week 7 of MN differentiation at RT using an inverted microscope (Zeiss). To identify MNs in our enriched cell cultures we applied strict selection criteria and included only multipolar neurons with large cell bodies as indicated by cell capacitances of at least ~20 pF. In brief, whole-cell currents were low-pass filtered and digitized at 2.9 kHz and 10 kHz using an EPC-10 amplifier (HEKA). PatchMaster and FitMaster software (HEKA) was used for recording and final analysis, respectively. Borosilicate glass pipettes (Science Products) were pulled to yield a resistance of 3-4 M $\Omega$  when filled with the internal solution (153 mM KCl, 1 mM MgCl<sub>2</sub>, 10 mM HEPES, 5 mM EGTA and 2 mM Mg-ATP, calibrated to pH 7.3 with KOH; 305 mOsm). The external bath solution contained 142 mM NaCl, 8 mM KCl, 1 mM CaCl<sub>2</sub>, 6 mM MgCl<sub>2</sub>, 10 mM glucose and 10 mM HEPES, calibrated to pH 7.4 with NaOH; 325 mOsm. Sodium and potassium ion currents were elicited by depolarizing voltage steps in increments of 10 mV from a holding potential of -70 to 40 mV. Miniature post-synaptic currents (mPSCs) were acquired at a holding potential of -70 mV in voltage clamp mode. Spontaneous and evoked action potentials were recorded in current-clamp mode.

## **RNA extraction and quantitative RT-PCR**

MNs were harvested after being cultured for 40-44 days. Total RNA was isolated using RNeasy columns (Qiagen) according to the manufacturer's instructions including a column DNase digest. CDNA-synthesis was performed with 250 ng of total RNA and the QuantiTect reverse transcription kit (Qiagen). Gene expression analysis was

performed by quantitative real-time PCR (qRT-PCR) using the power SYBR-green master mix (Life Technologies). Each well contained 1.4 µl primer mix (1.75pmol/µl; forward + reverse), 1.4 µl cDNA (1.75 ng/µl), 7 µl SYBR green master mix and 4.2 µl RNase free water. For measurements the StepONEPlus cycler (Applied Biosystems) was used with following cycling conditions: 95 °C/10 min. and 40 cycles à 95 °C/15 s and 60 °C/1 min. As recommended by the MIQE-guidelines (Bustin et al., 2009) specificity of PCR products was ensured by melting curve analysis and equal PCR efficiency of all primer pairs was validated by serial cDNA dilution. Data was analyzed with the qbase+ program (Andersen et al., 2004) using hypoxanthine-guanine phosphoribosyltransferase, TATA-binding protein and β-actin as reference genes. The following primers were used:

| Primer      | Sequence (5' →3')          |
|-------------|----------------------------|
| SMI32 fw    | GAGCTGAGGAACACCAAGTGGG     |
| SMI32 rev   | CTTCTGGAAGCGAGAAAGGAATTGGG |
| ChAT fw     | CCCGGAAATTCAAGGCCACTTAGC   |
| ChAT rev    | AGTCTTCGATGGAGCCTGTAGAAGG  |
| β-Actin fw  | CATGTACGTTGCTATCCAGGC      |
| β-Actin rev | CTCCTTAATGTACGCACGAT       |
| GAPDH fw    | AGCCACATCGCTCAGACACCAT     |
| GAPDH rev   | CAGGCGCCCAATACGACC AAAT    |
| HPRT1 fw    | AGACTTTGCTTTCCTTGGTCAGGC   |
| HPRT1 rev   | TGGCTTATATCCAACACTTCGTGGG  |
| TBP fw      | TCGGAGAGTTCTGGGATTGTA CCG  |
| TBP rev     | GGGATTATATTCGGCGTTTCG GGC  |
| MAP2 fw     | CAGGCAAAGGACAAAGTCTCTGACG  |
| MAP2 rev    | CGCCGAGGAGGGAGAATGGAGG     |

### **Quantification of *C9ORF72* isoforms, uORF, and antisense RNA**

Total RNA was extracted using the RNeasy kit (Qiagen, Hilden, Germany) and treated with DNase I according to the manufacturers' instructions. For each reaction, 250 ng of total RNA was reversely transcribed using QuantiTect reverse transcription kit (Qiagen, Hilden, Germany). Quantitative real-time PCR experiments were performed

with cDNA from 1.75 ng total RNA per reaction, 1.75  $\mu$ M forward and reverse primer and Power SYBR-Green PCR Master Mix (Life Technologies) in a StepOnePlus instrument (Applied Biosystems, Darmstadt, Germany) under the following amplification conditions: 95°C for 10 minutes, followed by 40 cycles of 95°C for 15 seconds and 60°C for 1 minute. The specificity of the PCR products was ensured by melting curve analysis. Equal PCR efficiency of all primer pairs was validated by serial cDNA dilution. For the quantification of target gene expression the threshold cycle (Ct) values of the targets were normalized against that of the endogenous references ACTB ( $\beta$ -Actin), HPRT1 (hypoxanthine phosphoribosyltransferase 1), TBP (TATA-box binding protein) and GAPDH (glyceraldehyde-3-phosphate dehydrogenase).

| Primer                | Sequence (5' $\rightarrow$ 3') |
|-----------------------|--------------------------------|
| antisense C9orf72-for | GGAGATGGAGTAAAGTGGACGATGGG     |
| antisense C9orf72-rev | GCCGTAGGCAAATGTCATTGTAGGG      |
| uORF-for              | CAAGAGCAGGTGTGGGTTTAGGAG       |
| uORF-rev              | GCGAGTACTGTGAGAGCAAGTAGTG      |
| ACTB-for              | CATGTACGTTGCTATCCAGGC          |
| ACTB-rev              | CTCCTTAATGTCACGCACGAT          |
| HPRT-for              | AGACTTTGCTTTCCTTGGTCAGGC       |
| HPRT-rev              | TGGCTTATATCCAACACTTCGTGGG      |
| TBP-for               | TCCGAGAGTTCTGGGATTGTACCG       |
| TBP-rev               | GGGATTATATTCGGCGTTTCGGGC       |
| GAPDH-for             | AGCCACATCGCTCAGACACCAT         |
| GAPDH-rev             | CAGGCGCCCAATACGACCAAAT         |

## RNA sequencing

For transcriptome sequencing (RNAseq), MNs of the cells lines C9-1, C9+KO-1 and C9GC-1 were generated in biological triplicates (3 independent differentiations side by side) and total RNA was isolated and validated as previously described. Next, mRNA was enriched with the NEBNext® Poly(A) mRNA Magnetic Isolation Module and sequencing libraries were prepared by following the protocol for NEBNext® Ultra II Directional RNA Library Prep Kit. This involves the following steps: mRNA

fragmentation, first strand and second strand cDNA synthesis, purification using the Agencourt® AMPure® Kit and end repair/dA-tailing of cDNA. Adapters were ligated to the dA-tailed cDNA, followed by a purification using AMPure XP Beads. Indexing of the library constructs was done with Illumina® index primer during the following PCR amplification using NEBNext® UltraII Q5 2X PCR Master Mix. Lastly, libraries were purified using the Agencourt® AMPure® Kit, equimolarly pooled and sequenced on an Illumina® NextSeq 550 system, resulting in ca. 29 – 36 million 75 bp single-end reads.

FastQC (v0.11.3) was used to perform a basic quality control on the sequence data. Reads were mapped to the human reference genome hg38 (obtained from Ensembl v87) using GSNAP (Wu and Nacu, 2010) (v2017-11-15) with splice-junction support from annotated genes (Ensembl v87). Further quality control on mapped reads, rRNA content, coverage of exonic/intronic/intergenic regions and number of detectable genes was done with RNA-SeQC (DeLuca et al., 2012) (v1.1.8). A table of raw read counts per gene was obtained based on the overlap of the uniquely mapped reads with annotated human genes (Ensembl v87) using featureCounts (Liao et al., 2014) (v1.5.3). Normalization of the raw read counts based on library size was performed with the DESeq2 R package (Love et al., 2014) (v1.16.1). Principle component analysis, sample-to-sample Euclidean distance as well as Pearson's and Spearman's correlation coefficients were computed based on the normalized gene expression level using R. For testing for differential expression with DESeq2, the count data was fitted to the negative binomial distribution and p-values for the statistical significance of the fold change were adjusted for multiple testing with the Benjamini-Hochberg correction for controlling the false discovery rate accepting a maximum of 5% false discoveries

(adjusted p-value  $\leq 0.05$ ) and log2fold change (FC)  $\geq 1$ . The lists of differentially expressed genes were used for gene ontology analysis using ENRICHR molecular function and DAVID (v.6.7). Data are deposited at NCBI/GEO under the accession numbers GSE143743 and GSE143744.

### **Spinal neuron characterization**

Expression levels of marker genes were determined by mRNA-sequencing (Amaryllis Nucleics, Oakland CA, USA). Reads were quantified as the transcript level using the software package Salmon (Patro et al., 2017) and the reference genome GRCH38 (ensembl.org) and summarized at the gene level with the R package tximport (Soneson et al., 2015). Reported values are regularized log counts (Love et al., 2014). Cell types were classified by a support vector machine trained on reference cell types derived from mouse (Sun et al., 2015) with PCA-computed eigengenes as features.

### **ELISA immunoassay**

To detect poly-GP DPR proteins, an ELISA immunoassay was performed with 3-week-old MNs lysed in RIPA buffer and processed as described (Lehmer et al., 2017).

### **REFERENCES**

Akimoto, C., Volk, A.E., van Blitterswijk, M., Van den Broeck, M., Leblond, C.S., Lumbroso, S., Camu, W., Neitzel, B., Onodera, O., van Rheen, W., *et al.* (2014). A blinded international study on the reliability of genetic testing for GGGGCC-repeat expansions in C9orf72 reveals marked differences in results among 14 laboratories. *J Med Genet* 51, 419-424.

Andersen, C.L., Jensen, J.L., and Orntoft, T.F. (2004). Normalization of real-time quantitative reverse transcription-PCR data: a model-based variance estimation approach to identify genes suited for normalization, applied to bladder and colon cancer data sets. *Cancer Res* 64, 5245-5250.

Bustin, S.A., Benes, V., Garson, J.A., Hellemans, J., Huggett, J., Kubista, M., Mueller, R., Nolan, T., Pfaffl, M.W., Shipley, G.L., *et al.* (2009). The MIQE guidelines:

minimum information for publication of quantitative real-time PCR experiments. *Clin Chem* 55, 611-622.

DeLuca, D.S., Levin, J.Z., Sivachenko, A., Fennell, T., Nazaire, M.D., Williams, C., Reich, M., Winckler, W., and Getz, G. (2012). RNA-SeQC: RNA-seq metrics for quality control and process optimization. *Bioinformatics* 28, 1530-1532.

Donnelly, Christopher J., Zhang, P.-W., Pham, Jacqueline T., Haeusler, Aaron R., Mistry, Nipun A., Vidensky, S., Daley, Elizabeth L., Poth, Erin M., Hoover, B., Fines, Daniel M., *et al.* (2013). RNA Toxicity from the ALS/FTD C9ORF72 Expansion Is Mitigated by Antisense Intervention. *Neuron* 80, 415-428.

Güven, G., Lohmann, E., Bras, J., Gibbs, J.R., Gurvit, H., Bilgic, B., Hanagasi, H., Rizzu, P., Heutink, P., Emre, M., *et al.* (2016). Mutation Frequency of the Major Frontotemporal Dementia Genes, MAPT, GRN and C9ORF72 in a Turkish Cohort of Dementia Patients. *PLoS One* 11, e0162592.

Jhanwar, S.C., Chen, Q., Li, F.P., Brennan, M.F., and Woodruff, J.M. (1994). Cytogenetic analysis of soft tissue sarcomas. *Cancer Genetics and Cytogenetics* 78, 138-144.

Lehmer, C., Oeckl, P., Weishaupt, J.H., Volk, A.E., Diehl - Schmid, J., Schroeter, M.L., Lauer, M., Kornhuber, J., Levin, J., Fassbender, K., *et al.* (2017). Poly - GP in cerebrospinal fluid links *C9orf72* - associated dipeptide repeat expression to the asymptomatic phase of ALS/FTD. *EMBO Molecular Medicine* 9, 859-868.

Liao, Y., Smyth, G.K., and Shi, W. (2014). featureCounts: an efficient general purpose program for assigning sequence reads to genomic features. *Bioinformatics* 30, 923-930.

Love, M.I., Huber, W., and Anders, S. (2014). Moderated estimation of fold change and dispersion for RNA-seq data with DESeq2. *Genome Biol* 15, 550.

Naujock, M., Stanslowsky, N., Bufler, S., Naumann, M., Reinhardt, P., Sternecker, J., Kefalakes, E., Kassebaum, C., Bursch, F., Lojewski, X., *et al.* (2016). 4-Aminopyridine Induced Activity Rescues Hypoexcitable Motor Neurons from Amyotrophic Lateral Sclerosis Patient-Derived Induced Pluripotent Stem Cells: 4AP rescues ALS iPSC derived motor neurons. *STEM CELLS* 34, 1563-1575.

Naumann, M., Pal, A., Goswami, A., Lojewski, X., Japtok, J., Vehlow, A., Naujock, M., Günther, R., Jin, M., Stanslowsky, N., *et al.* (2018). Impaired DNA damage response signaling by FUS-NLS mutations leads to neurodegeneration and FUS aggregate formation. *Nature Communications* 9.

Patro, R., Duggal, G., Love, M.I., Irizarry, R.A., and Kingsford, C. (2017). Salmon provides fast and bias-aware quantification of transcript expression. *Nat Methods* 14, 417-419.

Selvaraj, B.T., Livesey, M.R., Zhao, C., Gregory, J.M., James, O.T., Cleary, E.M., Chouhan, A.K., Gane, A.B., Perkins, E.M., Dando, O., *et al.* (2018). C9ORF72 repeat expansion causes vulnerability of motor neurons to Ca<sup>2+</sup>-permeable AMPA receptor-mediated excitotoxicity. *Nat Commun* 9, 347.

Sivadasan, R., Hornburg, D., Drepper, C., Frank, N., Jablonka, S., Hansel, A., Lojewski, X., Sternecker, J., Hermann, A., Shaw, P.J., *et al.* (2016). C9ORF72 interaction with cofilin modulates actin dynamics in motor neurons. *Nat Neurosci* 19, 1610-1618.

Soneson, C., Love, M.I., and Robinson, M.D. (2015). Differential analyses for RNA-seq: transcript-level estimates improve gene-level inferences. *F1000Res* 4, 1521.

Sun, S., Sun, Y., Ling, S.C., Ferraiuolo, L., McAlonis-Downes, M., Zou, Y., Drenner, K., Wang, Y., Ditsworth, D., Tokunaga, S., *et al.* (2015). Translational profiling

identifies a cascade of damage initiated in motor neurons and spreading to glia in mutant SOD1-mediated ALS. *Proc Natl Acad Sci U S A* 112, E6993-7002.

Wu, T.D., and Nacu, S. (2010). Fast and SNP-tolerant detection of complex variants and splicing in short reads. *Bioinformatics* 26, 873-881.